Characterization of Ti-5553 parts printed by Selective Laser Melting (SLM)

by

Soheil Bakhshivash

A thesis
presented to the University of Waterloo
in fulfillment of the
thesis requirement for the degree of
Master of Applied Science
in
Mechanical and Mechatronics Engineering

Waterloo, Ontario, Canada, 2018

I hereby declare that I am the sole author of this thesis. This is a true copy of the thesis, including any required final revisions, as accepted by my examiners.

I understand that my thesis may be made electronically available to the public.

Abstract

Nowadays, titanium alloys are widely used in a variety of industries like automotive and aerospace due to their high strength to weight ratio. Ti-5%Al-5%V-5%Mo-3%Cr is a metastable near beta titanium alloy with excellent fatigue performance and corrosion resistance. Hence, it is mainly used in the airframe structure and the landing gear components. As the additive manufacturing (AM) industry grows everyday, so does the interest in printing of strategic Titanium alloys. Selective Laser Melting (SLM) is a powder-bed fusion process utilizing the laser power as the heat source which scans over a compact powder layer along a pre-defined path. In this study, the printability of Ti-5553 by pulsed-laser SLM is investigated, thoroughly. To this end, a batch of powder was first characterized in terms of size distribution, porosity level, chemical composition and microstructure. Afterwards, the effect of Volumetric Energy Density (VED), sample geometry and scanning strategy was evaluated on the microstructure and properties of the printed parts. Various tests such as Archimedes method, Nano-CT scanning, surface roughness, Optical Microscopy (OM), Scanning Electron Microscopy (SEM), Transmission Electron Microscopy (TEM), X-ray diffraction (XRD), Electron backscattered diffraction (EBSD) and hardness mapping were applied. Results showed that the virgin plasma-atomized powder had a high quality with a mean sphericity of 0.95 and porosity of less than 0.01%. In addition, it was observed that there was an optimized VED range leading to a nearly fully dense part, *i.e.* 99.7%, with a smooth surface. Low and High VEDs resulted in a lack of fusion and spattering, respectively, both undermining the density of the printed parts. Moreover, high VEDs provided the energy required for the beta to alpha transformation and caused in-situ precipitation hardening. This in-situ heat treatment is not desired due to the lack of homogeneity. Furthermore, the sample geometry, *i.e.* cubic or cylindrical, was determined to have negligible effects on the achieved properties while the choice of scanning strategy directly affected the texture and density of the printed parts. It was seen that the chessboard, stripes and total fill strategies led to the optimized, medium and poor properties, respectively. Finally, the best density of 99.94% was achieved by using the VED of $112\,\mathrm{J/mm^3}$ and the chessboard scanning strategy. The sample showed a homogeneous hardness distribution with an average of 295 $\pm$10 HV. The TEM analysis determined that the sample was in the beta to omega phase transformation stage. Also, it had a columnar grain structure elongated parallel to the building direction indicating a highly crystallographically textured part. The EBSD analysis supported these findings by suggesting a preferred growth direction with crystal texture seven times higher than the random intensity. The melt pool shape of the optimized sample was seen to be goblet-like with a lower penetration compared to the sample printed by the stripes strategy.

Acknowledgements

My immense thanks go to all of the following:

Dr. Adrian Gerlich for being such a great supervisor. Adrian was more than a mentor to me. He is an amazing boss, friend, colleague and role model to his students. I learnt a lot from him both in technical work and life lessons. I was so lucky to be in his research team. He does really care about his students and always meets their concerns. With his excellent management, I was able to successfully prosper with no fear of being overstressed.

Prof. Ehsan Toyserkani who trusted me and kindly welcomed me to his research team. His patience and guidance helped me to work in the research field that I was interested in with a minimal stress level. His technical knowledge regarding the topic was always a key factor to my success.

Dr. Hamed Asgari who was the best mentor I could ever wish for. His knowledge and prompt response to my questions always encouraged me. I thank him for his supervision over technical aspects of the project including microstructural evolution, hardness and density.

Dr. Paola Russo who put so much effort to design and develop the screening phase. I'd like to thank her for the perseverance and support.

My lovely family who always supported me during the hard times. I wouldn't be able to do any of this without their encouragement. The love and guidance I've always received from my mom, dad and my younger brother, Sepehr, has always helped to to make the right choices and to never give up on my dreams.

Parisa, the love of my life, for being such an incredible supporter and the best wife anyone can imagine. Her patience and love were the best blessings when the tasks seemed overwhelming and my greatest motivation was always to be with her sooner.

Dedication

To

Parisa,
Sepehr,
Mom,
Dad,

& all the ones I love!

Table of Contents

List of Tables ix

List of Figures x

Abbreviations xiv

1 Introduction 1

1.1 Additive manufacturing industry 1

1.2 Pros and cons of AM 1

1.3 Applications of AM in aerospace 2

1.4 Titanium alloys in aerospace 3

1.5 Challenges associated with AM in aerospace 3

1.6 Aims of the research 4

1.7 Thesis outline 4

2 Literature review 5

2.1 Metallurgy of Titanium alloys 5

2.1.1 History of Titanium 5

2.1.2 Crystal structure 6

2.1.3 Effect of alloying elements 7

2.1.4 Beta Titanium alloys 9

2.2 Additive manufacturing . . . 11
2.2.1 Classification . . . 11
2.2.2 Selective laser melting . . . 12
2.2.3 Volumetric energy density . . . 13
2.2.4 Scanning strategies . . . 13
2.3 AM using Ti-5553 alloy powder . . . 14

3 Experimental procedure **18**
3.1 Materials . . . 18
3.1.1 Ti-5553 powder . . . 18
3.1.2 Kroll's reagent . . . 19
3.2 Equipment . . . 20
3.2.1 Renishaw SLM machine . . . 20
3.2.2 ZEISS Nano-CT scanner . . . 21
3.2.3 Keyence confocal microscope . . . 21
3.2.4 FT4 powder rheometer . . . 21
3.2.5 ZEISS Ultra SEM . . . 22
3.2.6 JEOL 2010F TEM . . . 22
3.2.7 Bruker D8 XRD machine . . . 22
3.2.8 CLEMEX CMT . . . 22
3.3 Methodology . . . 23

4 Selective laser melting of Ti-5553 **28**
4.1 Powder characterization . . . 28
4.2 Effect of volumetric energy density . . . 35
4.3 Effect gemetry and scanning strategy . . . 57

5 Conclusion **64**

6 Future works **66**

References **67**

List of Tables

2.1 Pros and cons of β Titanium alloys 9
2.2 Metall additive manufacturing classification 11
2.3 The advantages and disadvantages associated with each scanning strategy . 14

3.1 Particle size distribution analysis results 18
3.2 Chemical composition of the virgin Ti-5553 powder 19
3.3 The chemical composition of Kroll's reagent 19
3.4 List of parameters chosen to print the first batch of samples 24
3.5 The sample preparation procedure used for Ti-5553 26
3.6 List of sample specifications for the second printing batch 27

4.1 The summary of the image analysis results 32
4.2 The Energy-dispersive X-ray Spectroscopy (EDS) analysis results done on the powder sample 32
4.3 The Rockwell hardness test results performed on the low, best and high Volumetric Energy Density (VED) samples 42
4.4 Rockwell hardness test results performed on the samples printed by the Stripes, Chessboard and Total fill scanning strategies 59

List of Figures

2.1 (a) the HCP and (b) the BCC crystal structures of Titanium with their most densely packed lattice planes [1]. 6

2.2 Effect of alloying elements on the β to α transition temperature [1]. 7

2.3 Schematic illustration of a psudo-binary phase diagram showing the effect of β stabilizer content on the type of Titanium alloy [1]. 8

2.4 Ti-6554 aged for (a) 10 min at 773 K, (b) 6 hr at 573 K followed by 10 min at 773 K, (c) 12 hr at 573 K followed by 10 min at 773 K, (d) 24 hr at 573 K followed by 10 min at 773 K. [2] 10

2.5 The schematic illustration of the glsslm process [3]. 12

2.6 Nano-CT scan results showing (a) the sample with the hatching overlap of 60 µm and (b) the sample with the optimized hatching overlap of 120 µm [4]. 15

2.7 The EBSD results showing the texture in (a) the front cross-section and (b) the top view, respectively [4]. 15

2.8 The surface roughness study results showing the effect of powder size range on the final roughness achieved [5]. 16

2.9 The heat treatment cycle used [6]. 17

2.10 The effect of in-situ heat tratment on the α phase content of the printed samples [6]. 17

3.1 The modulated laser powder-bed additive manufacturing machine used [7]. 20

3.2 The different scanning strategies provided by the Renishaw machine. . . . 21

3.3 The input CAD file showing the random distribution of the samples on the first printing batch build plate. 25

3.4 The input CAD file showing the random distribution of the samples on the second printing batch build plate. 26

4.1 The results for three repeat sets of samples showing (a) the compressibility and (b) the permeability of the as-received Ti-5553 powder. 29

4.2 Scanning Electron Microscopy (SEM) images taken from the virgin powder using low (a and b) and high (c and d) magnifications. 30

4.3 Two examples of the non-spherical particles observed. 31

4.4 Ultra-fine particles partially fused to the interface of larger ones. 31

4.5 The image analysis results showing (a) the size distribution and (b) the sphericity of the powder particles. 32

4.6 The SEM observations revealing inside of the particles. 33

4.7 The Nano-CT scan test results showing (a) the powder particles and (b) their internal pores. 34

4.8 The X-ray Diffraction (XRD) results performed on the virgin powder. . . . 34

4.9 The as-printed batch showing (a) the random distribution of the samples and (b) the burned surface of the sample with high VED. 35

4.10 Effect of VED on relative density of fabricated Ti-5553 specimens. 36

4.11 The Archimedes density analysis results showing the effect of (a) laser power, (b) scanning velocity, (c) point distance and (d) exposure time on the relative density achieved. 37

4.12 The Nano-CT scan results showing (a) the size distribution and (b) morphology of the internal porosities for the samples with the best and highest VEDs used. 38

4.13 The quantitative Nano-CT scan results showing (a) the pore size distribution and (b) the sphericity of them. 39

4.14 Effect of VED on the surface roughness of the printed samples. 40

4.15 The color map contours showing the effect of exposure time and point distance on surface roughness while using different laser powers. 41

4.16 The XRD results comparing the samples with the best and the highest VEDs. 42

4.17 The stereo microscopy images showing the porosity level and surface condition of the printed samples sectioned along their diameter. 43

4.18 The stereo microscopy images showing the porosity level and surface condition of the printed samples in top view. 44
4.19 The micro-hardness color maps showing (a) sample 20 and (b) sample 27 at the front view. 45
4.20 The front view Optical Microscopy (OM) images showing (a) the lowest VED, (b) the highest VED and (c) the best density samples, respectively. . 46
4.21 The top view OM images showing (a) the lowest VED, (b) the highest VED and (c) the best density samples, respectively. 47
4.22 The SEM images showing (a) unmelted powders, (b) partially melted powders and (c) embedded powders, respectively. 48
4.23 The SEM images showing the precipitate particles in (a) low and (b) high magnifications. 49
4.24 The SEM images taken from the best density sample showing (a) the epitaxial growth of grains, (b) the transition in the solidification mechanism around the melt pool edges and (c) the embedded powders, respectively. . 50
4.25 The Transmission Electron Microscopy (TEM) images taken from the best density sample showing (a) the stacking faults, (b) the HCP omega phase particles and (c) the lattice strains, respectively. 51
4.26 The omega phase detection by TEM (a) the image taken from the SAD and (b) the diffraction pattern. 52
4.27 The TEM images showing the alpha phase structures in (a) the top and (b) the bottom part of the sample with the highest VED, respectively. 53
4.28 The TEM observation of the alpha phase showing (a) the image taken from the SAD and (b) the the corresponding diffraction pattern, respectively. . . 54
4.29 The TEM/EDAX color map showing the distribution of the alloying elements in the high VED sample. 54
4.30 The comparison between the diffraction patterns of the pure beta phase matrix and the general overview of the structure: (a) the TEM image showing the SADs, (b) the diffraction pattern of SAD 1 showing a pure beta phase, (c) the diffraction pattern of SAD 2 showing the coherent alpha phase along with the matrix and (d) the detailed schematic illustration of the alpha phase pattern distribution in c. 55

4.31 The IPF color map showing the texture of the top surface of the best density sample. 56
4.32 The pole figures of (a) the BCC and (b) the HCP phases, respectively. . . 56
4.33 The second printing batch showing the build plate (a) during the process and (b) after the process, respectively. 57
4.34 The effect of using different scanning strategies and geometries on the relative density. 58
4.35 The Nano-CT scan results showing the pore volume distribution when using (a) the stripes and (b) the chessboard scanning strategies, respectively. . . 59
4.36 The stereo microscopy images showing the porosity level and surface condition of the printed samples with different scanning strategies in front view. 60
4.37 The stereo microscopy images showing the porosity level and surface condition of the printed samples with different scanning strategies along the top view. 60
4.38 The front view OM images showing the samples printed by (a) the strips, (b) the chessboard and (c) the total fill scanning strategies, respectively. . . 61
4.39 The OM observations showing the melt pool geometries of (a) the stripes and (b) the chessboard scanning strategies, respectively. 62
4.40 The top view OM images showing the samples printed by (a) the strips, (b) the chessboard and (c) the total fill scanning strategies, respectively. 63

Abbreviations

AM Additive Manufacturing 1–4, 11, 16

EBSD Electron Backscattered Diffraction 4, 14, 27, 28, 57, 63, 64, 66

EDS Energy-dispersive X-ray Spectroscopy ix, 22, 31, 32

OM Optical Microscopy xii, xiii, 4, 22, 25, 27, 28, 45–47, 61–64

SEM Scanning Electron Microscopy xi, xii, 4, 14, 22, 23, 25, 27–31, 33, 47–50, 64

SLM Selective Laser Melting 4, 5, 12, 14–16, 23, 64–66

TEM Transmission Electron Microscopy xii, 4, 10, 16, 22, 25, 28, 47, 49–55, 57, 64, 66

VED Volumetric Energy Density ix, xi, xii, 4, 13, 23, 25, 35, 36, 38–47, 49, 52–54, 57, 58, 62, 64, 66

XRD X-ray Diffraction xi, 4, 16, 22, 23, 25, 28, 32–34, 42, 57, 64, 66

Chapter 1

Introduction

1.1 Additive manufacturing industry

Additive Manufacturing (AM) is defined as "a process of joining materials to make objects from 3D model data, usually layer upon layer, as opposed to subtractive manufacturing methodologies. Synonyms [include]: additive fabrication, additive processes, additive techniques, additive layer manufacturing, layer manufacturing, and freeform fabrication" [8]. Although the first 3D printing process was introduced in 1987 by the commercialization of stereo-lithography, the metal additive manufacturing initially emerged not sooner than 1998 [9]. After two decades, the industry is growing to become an important means of commercial production technology [10]. Statistics show a significant increase in the global AM market size from $5.2 billion in 2015 to $12.4 billion in 2018 [11].

1.2 Pros and cons of AM

Three key industries of automotive, aerospace and medical, have invested heavily on AM technology [12]. The benefits of AM for each is presented below:

- **Automotive:** One of the main applications of AM in the automotive industry is tool making. It gives the car manufacturers the chance to produce specialized assembly devices. Thanks to its ability to print free-form shapes, AM gives tool designers the chance to enhance the performance and handling characteristics [13].

- **Aerospace:** The main features that makes the AM processes attractive for the aerospace industry are the ability to make parts with no tools required which speeds up the production rate and reduces the cost. In addition, these processes provide a more straightforward supply chain [14]
- **Medical:** AM is revolutionizing the medical industry in terms of modeling a bone structure before a surgery with the goal of making an exact transplant regardless of the complexity [15].

Like any other manufacturing process, AM has its own drawbacks which are listed below:

- **Size:** There is a size limit associated with AM. As the processes are relatively slow, it is not practical to make very large parts [16].
- **Defects:** It is hard to eliminate defects such as porosity, micro-cracks and rough surface. In most cases, post processing, in terms of Hot Isostatic Pressing (HIP), machining and heat-treatment, is required.
- **Cost:** It is very expensive to purchase and maintain an AM machine. With the price range of usually more than $200K, they are expensive to be invest on.

1.3 Applications of AM in aerospace

Aerospace parts are sometimes complex. In addition, the materials used in the aerospace industry are usually expensive and it is important to minimize the waste. These factors give rise to the industrial use of AM. General applications of AM in the aerospace industry fall into three categories of component manufacturing, tool making and repair [17]. Several applications of AM in the aerospace industry are listed below:

- Airframe components
- Landing gear components
- Compressor support case
- Engine cases
- Engine blades
- Engine housing

1.4 Titanium alloys in aerospace

Titanium alloys are widely used in the aerospace industry due to a combination of high strength to weight ratio, corrosion resistance, good creep resistance of up to 550 °C and excellent fatigue performance. The following are some of the key reasons why Titanium alloys are popular [18]:

- weight reduction,
- high service temperature,
- polymer matrix composite compatibility,
- corrosion resistance,
- tolerance to cyclic loading.

In most cases, Titanium alloys are a good replacement for aluminum, and sometimes, nickel based alloys in aircraft. In fact, 20% of a Boeing 787's weight is made of Titanium alloys as a consequence of the above mentioned characteristics [19, 1].

1.5 Challenges associated with AM in aerospace

Although AM seems to be a good fit for manufacturing a variety of aerospace components, there are concerns that need to be met and questions to be answered. Some of the challenged accompanied with AM in aerospace are [20]:

- **Process sensitivity:** There are various AM processes. One needs to learn manipulate the machine-to-machine variability.
- **Means of inspection:** If one decides to utilize AM processes, they must develop new standards and introduce advanced inspection tools for non-destructive testing (NDT).
- **Design:** As innovations are made regarding the structural characteristics, new design guidelines are required to decrease weight parts.
- **Modeling:** The physics associated with AM needs to be modeled, accurately, with the goal of precise microstructure and properties predictions. The models can facilitate the process optimization.

1.6 Aims of the research

This research covers the printability of Ti-5%Al-5%V-5%Mo-3%Cr by focusing on microstructural evolution occurring during pulsed laser Selective Laser Melting (SLM) and the effects of VED, sample geometry and scanning strategy on it. The results discussed are a part of a longer term project and are considered as a preliminary screening phase with the goal of achieving a basic understanding of both the material and the process. The core objective of this thesis is to optimize the microstructure and also to achieve a reasonable density, roughness and hardness. The design of experiment (DOE) or the statistical analysis stages are presented elsewhere.

1.7 Thesis outline

This thesis is divided into literature review, materials and methods followed by a chapter dedicated to the results and discussion. A brief summary of the findings and potential approaches to reach a more comprehensive results are give in the conclusions and future works chapters, respectively.

The literature review provides a general understanding of AM and SLM in particular. Also, basics of metallurgy of Titanium alloys are discussed in detail with a focus on metastable beta alloys. Finally, a review on the AM of Ti-5553 is given. The materials, equipment and methodology used, including the chamistry and size distribution of the as-received powder, metallography sample preparation, characterization and processing equipment, design of experiment, etc., in the research are explained in deep in Chapter 3. The research findings, *i.e.* the density, surface roughness, hardness, OM, SEM, TEM, Electron Backscattered Diffraction (EBSD) and XRD results,are presented in Chapter 4 and a deep discussion is given for each with the goal of optimizing the process-microstructure-properties relations. Finally, the main takeaways and potential research areas are clarified in Chapters 5 and 6, respectively.

Chapter 2

Literature review

In this chapter, a brief review of the principles of metallurgy of Titanium alloys as well as basics of pulsed-laser SLM is given. In addition, several previous attempts to assess the printability of Ti-5553 are presented and their findings are discussed, thoroughly.

2.1 Metallurgy of Titanium alloys

2.1.1 History of Titanium

Titanium, as the fourth most abundant elemnt in earth's crust, can be found naturally as two compounds of TiO_2, *i.e.* rutile, and $FeTiO_3$ or ilmenite. Titanium was first detected as an unknown element present in rutile by William Gregor in in 1791. Four years later, a German scientist called Klaproth announced that Rutile is an oxide for a new element and he called the element Titaium [1].

Many attempts were taken in order to obtain pure Titanium. Around 1937, Krolls succeeded in purifying Titanium by the reduction of $TiCl_4$ with Mg in an inert environment [1]. The first Titanium alloys emerged almost three years later in 1940 [21]. That was when the commercial usage of Titanium in industries like aerospace and defence started to grow as they needed a rather strong alloy with a relatively lower density to be used in the engine and airframe structural components [22].

The Dupont company was the first of its kind that commercialized Titanium products in 1948 [21]. The aerospace industry is still the main consumer of Titanium alloys, however, other markets like automotive, medical and architecture are using them. Titanium is

difficult and expensive to process, consequently, not all industries can economically utilize Titanium based alloys.

2.1.2 Crystal structure

Pure Titanium has an allotropic transformation at 882 °C above which it has a BCC structure, *i.e.* the β phase, with the lattice parameter of 0.332 nm. When it cools down to below the transformation temperature, it turns into an HCP phase called the α phase which has lattice parameters of a = 0.295 nm and c = 0.468 nm [1]. Figure 2.1 shows the mentioned phases. The HCP structure, see Figure 2.1a, has three close packed planes of basal, prismatic and pyramidal, *i.e.* (0002), the $\{10\bar{1}0\}$ family and the $\{10\bar{1}1\}$ family, respectively. On the other hand, the BCC structure has only one close packed plane family of {110} as shown in Figure 2.1b.

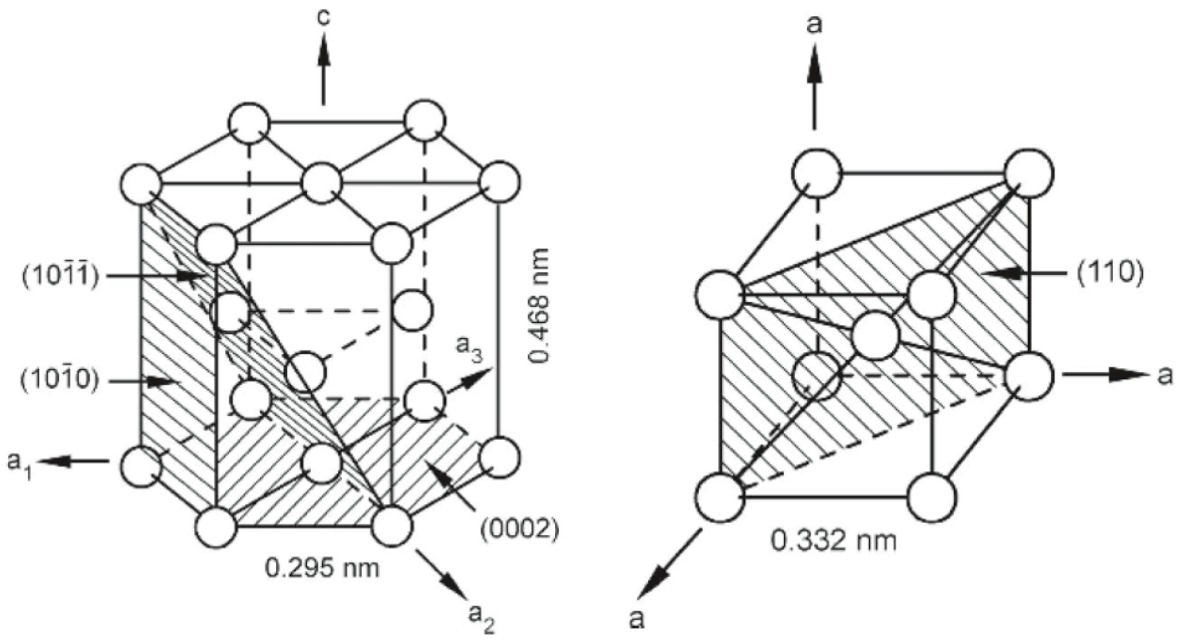

(a) (b)

Figure 2.1: (a) the HCP and (b) the BCC crystal structures of Titanium with their most densely packed lattice planes [1].

2.1.3 Effect of alloying elements

As shown in Figure 2.2, there are three main types of alloying elements classified based on their effect on the allotropic transition temperature. The first group, *i.e.* the α stabilizers, increase the transition temperature. Aluminum is the most popular α stabilizer being used in Titanium alloys. On the other hand, the β stabilizers decrease the transition temperature. Based on the way they work, they fall into two categories of β-isomorphous and β-eutectoid elements. Finally, neutral elements such as Zirconium and Tin have no effect of the β to α transformation.

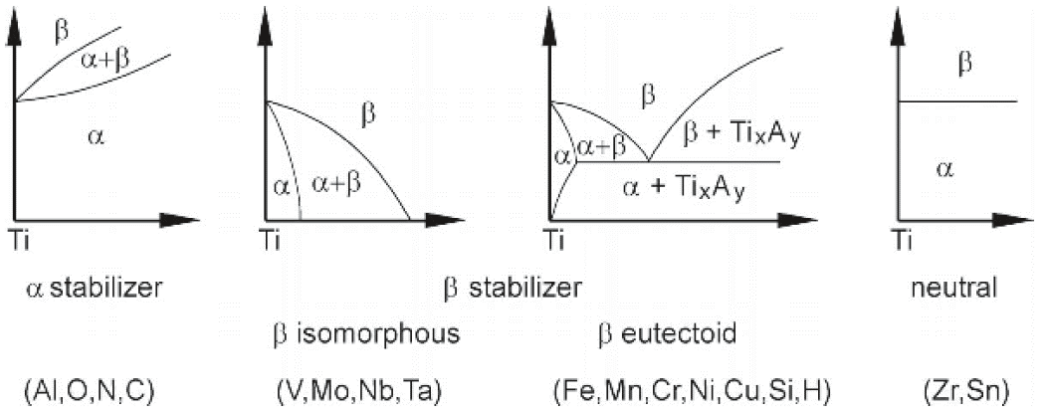

Figure 2.2: Effect of alloying elements on the β to α transition temperature [1].

According to the alloying elements used, Titanium alloys can be classified as follows [23]:

- α alloys
- near α alloys
- $\alpha + \beta$ alloys
- near β alloys
- β alloys

When more than one alloying element is used, usually an Aluminum or Molybdenum equivalent, as described in Equations 2.1 and 2.2, is used to assess the effect of α and β stabilizers, respectively [17].

$$[Al]_{equiv.} = [Al] + 0.17[Zr] + 0.33[Sn] + 10[O] \tag{2.1}$$

$$[Mo]_{equiv.} = [Mo] + 0.67[V] + 2.9[Fe] + 1.6[Cr] \tag{2.2}$$

The binary phase diagram shown in Figure 2.3 clarifies the effect of β stabilizers on the Titanium alloy classification. α stabilizers affect the diagram in exact opposite way. Ti-5553 has 4 main alloying elements, *i.e.* Aluminum, Vanadium, Molybdenum and Chromium. One may notice that three of these elements are considered as β stabilizer. Hence, this alloy is also known as a near β,or metastable β, Titanium alloy. Since this project focuses on using Ti-5553, a brief introduction to β alloys is given in the following section.

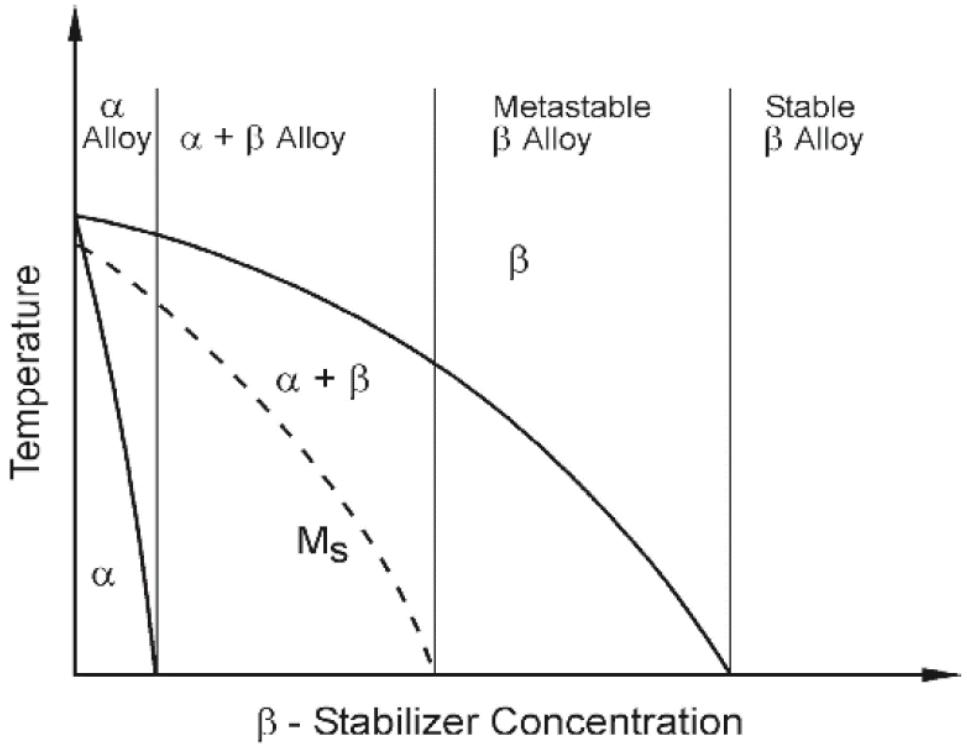

Figure 2.3: Schematic illustration of a psudo-binary phase diagram showing the effect of β stabilizer content on the type of Titanium alloy [1].

2.1.4 Beta Titanium alloys

Table 2.1 shows some of the pros and cons of β Titanium alloys compared to other categories [21]. These alloys are the most expensive and strongest Titanium alloys.

Table 2.1: Pros and cons of β Titanium alloys

Pros	Cons
high specific strength	higher density
excellent fatigue performance	small processing window
cold formable	high cost
easy to harden	segregation issues

The high content of β stabilizers in these alloys, *i.e.* usually more than 10%, suppresses the martensitic transformation commonly seen in the $\alpha + \beta$ Titanium alloys. Some conventional heat-treating processes used for β Titanium alloys are [21]:

- β solution annealing
- α/β solution annealing
- short-term high temperature exposure
- long term low temperature exposure

By solution annealing above the allotropic transition temperature, a pure β microstructure with a coarse grain structure is achievable. On the other hand, if the solution annealing takes place at the temperatures slightly lower than that of the β transus, needle-shaped primary α (α_p) precipitates. Another type of α precipitates is the grain boundary α (α_{GB}). Since the grain boundaries have a higher energy state compared to the matrix, they are preferred nucleation sites for the secondary phase precipitation, which in this case is α phase[21].

By warming a Ti-5553 sample up to temperatures near 400 °C, a fine distribution of the secondary α needles, *i.e.* α_s, can be achieved within the matrix. The presence of such precipitates increases the hardness and strength of the material, significantly. The aging temperature and time determines the size and distribution of the precipitates which, in turn, defines the mechanical response of the material. In sum, three key factors of β grain

size, grain boundary α and the morphology and volume fraction of α_p and α_s must be carefully controlled in order to reach the desired properties [21].

The β to α transformation has two steps. First, an HCP phase called ω with a short c/a ratio nucleates at the early stages of aging. While the precipitation pace is controlled by the aging temperature and time, the nano-scale equiaxed ω phase next turns into the α needles with a basket-wave structure. Figure 2.4 shows a few dark field TEM images taken from an Ti-6554 alloy in different aging conditions. The transition between the ω

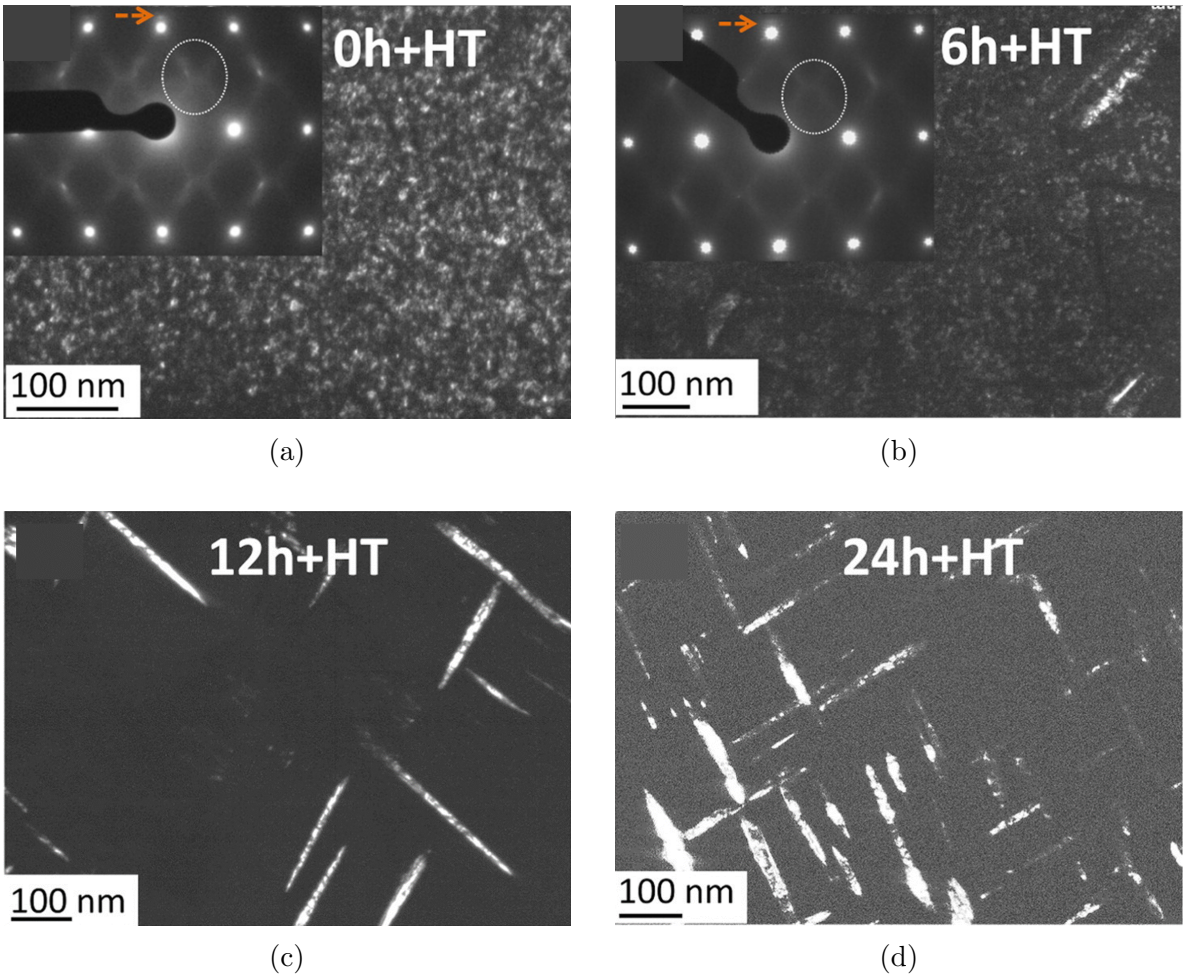

Figure 2.4: Ti-6554 aged for (a) 10 min at 773 K, (b) 6 hr at 573 K followed by 10 min at 773 K, (c) 12 hr at 573 K followed by 10 min at 773 K, (d) 24 hr at 573 K followed by 10 min at 773 K. [2]

to α phase can be clearly seen. In summary, the general allotropic transformation can be written as $\beta \rightarrow \beta + \omega \rightarrow \beta + \alpha$.

2.2 Additive manufacturing

2.2.1 Classification

Additive manufacturing (AM) is a rather new technique capable of printing parts layer by layer to a near net-shape geometry with minimal machining required. Various AM processes utilize different heat sources such as plasma arc, laser and electron beam to melt or sinter a powder bed layer, wire or ribbons [24, 25, 26, 27, 28].

First, a CAD file is broken into many sections. Each of the sections next will be used to print the parts layer by layer in an inert or vacuum atmosphere [17]. The AM, formerly known as 3D printing or rapid prototyping, has been used for a few decades. Nowadays industries like aerospace, automotive, defence and medical are showing an increasing demand for applying this technology to make their products [29, 30, 31, 32].

AM processes can be classified based on their heat source or their feed stock. Table 2.2 shows some of the processes used in each source-feed stock combination. Each process has its own advantages and drawbacks. For instance, the wire-feed systems have a higher

Table 2.2: Metall additive manufacturing classification

Heat source	Feedstock	Examples
Laser	Powder-bed	SLM SLS
	Powder-fed	DMD LENS
	Wire	SMD
Arc	Powder-bed	-
	Powder-fed	-
	Wire	WAALM
Electron beam	Powder-bed	EBSM
	Powder-fed	-
	Wire	EBF

deposition rate which improves the manufacturing time, however, the dimensional accuracy is a challenge for them. In other words, more machining, leading to higher amount of waste, is needed to finish their surface. The systems using an electron beam source need a vacuum environment and also usually need a pre-heated substrate for better results. Thus, such processes are more time consuming and expensive but they are good for the production of larger parts, *e.g.* an engine blade. One should choose the best process based on the material, part size, time and application.

2.2.2 Selective laser melting

Selective laser melting (SLM) is a powder-bed fusion system utilizing the laser power as the heat source. As shown in Figure 2.5, the laser is directed by a mirror to scan over a path defined by the CAD file and melts a powder layer. Once the scanning phase is complete, the fabrication piston moves down by a thickness of a powder layer which is distributed by a roller on the previous layer, homogeneously.

There are two different categories of SLM processes: (I) continuous laser and (II) pulsed laser. The melt pool geometry can be controlled easily by the latter.

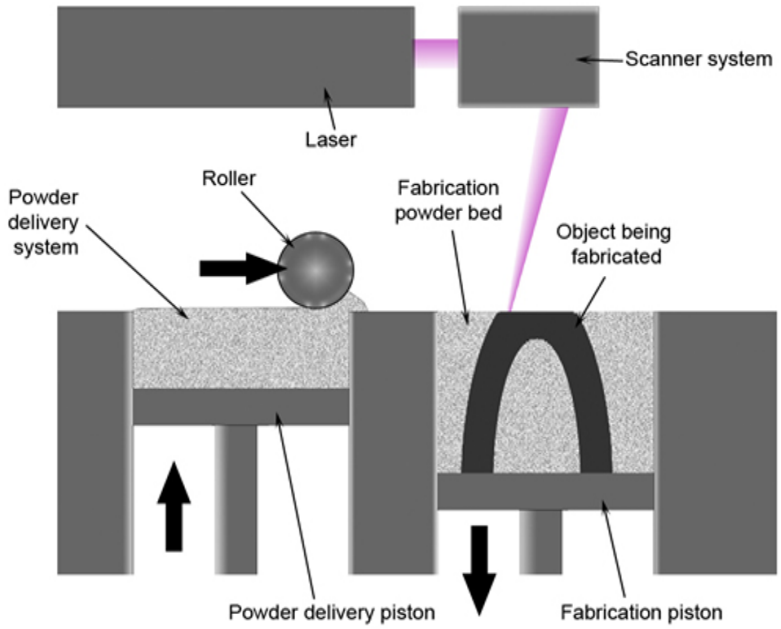

Figure 2.5: The schematic illustration of the glsslm process [3].

2.2.3 Volumetric energy density

Volumetric energy density (VED) is defined as the average energy transferred to a volume of material and usually expressed as J/mm. It is one of the key factors playing an important role in the quality of the printed components. Hence, the first step to build a recipe is to optimize the VED. Equation 2.3 presents the general formula to calculate the VED:

$$VED_{(\mathrm{J/mm^3})} = \frac{P}{vdl} \tag{2.3}$$

where P is the laser power, v is the laser scanning velocity, d is the laser spot diameter and l represents the layer thickness. When a pulsed laser system is used, the laser scanning velocity itself is dependant to the point distance p_d and exposure time e_t as shown below by Equation 2.4 [33]:

$$v_{(\mathrm{m/s})} = \frac{p_{\mathrm{d}}}{e_{\mathrm{t}}} \tag{2.4}$$

By combining the above equations, the VED in pulsed laser systems can be calculated by Equation 2.5:

$$VED_{(\mathrm{J/mm^3})} = \frac{Pe_{\mathrm{t}}}{p_{\mathrm{d}}dl} \tag{2.5}$$

Amongst these parameters, the laser spot diameter and layer thickness are usually kept constant for all of the samples. Hence, the three parameters of laser power, point distance and exposure time must be modified in order to optimize the properties of the printed components.

2.2.4 Scanning strategies

Another factor determining the quality of the results is the laser scanning strategy chosen. There are a variety of strategies available depending on the machine used. The four most popular strategies are: (I) stripes, (II) chessboard, (III) total fill and (IV) meander. Each strategy has its own advantages and disadvantages. Table 2.3 shows the pros and cons of each strategy. One should consider the size and geometry of the part to be printed before choosing the scanning strategy.

Table 2.3: The advantages and disadvantages associated with each scanning strategy

Strategy	Advantages	Disadvantages
Stripes	Consistent heat distribution throughout the layer Ideal for parts with large XY cross-section	Rather slow
Chessboard	Improvements over Stripes	Slower than Stripes
Total fill	Good surface finish	Poor density
Meander	Quick and efficient Ideal for parts with small XY cross-section	Inconsistent heat distribution

2.3 AM using Ti-5553 alloy powder

By the time of this thesis, there are only three research articles available addressing the SLM of Ti-5553. In this section, each paper is discussed, briefly.

The first article is written by Shwab *et al.* [4] which focuses on continuous SLM of a gas-atomized Ti-5553 powder with the size range of 25-45 µm and a pure β phase structure. While keeping the laser spot diameter at 80 µm, five different laser powers of 60, 80, 100, 120 and 140 W were used along with five scanning velocities of 100, 120, 140, 160 and 180 mm/s. In addition, two scanning strategies of stripes and chessboard were investigated. Cylindrical and cubic samples were printed for the tensile tests and characterization, respectively.

The papers suggests that the best result, in terms of density, was achieved by using the laser power of 100 W and the scanning velocity of 180 mm/s. Also the chessboard strategy led to a significantly better results. Figure 2.6 shows the effect of hatching overlap on the final density. It is found that by optimizing the overlap field, the porosity level drops from 0.11% to 0.05%.

In addition, a columnar grain structure is seen parallel to the building direction by EBSD analysis, see Figure 2.7. It is explained that the reason of this highly textured structure is the re-melting cycles applied to the beneath layers. Also the mean grain width is determined to be 140 µm.

Figure 2.7 also demonstrates that the grain structure is much finer at the scanning track overlaps compared to the coarser grains inside each track. It is discussed that there is an intense texture occurred along the 100 plane family with 7 times the random intensity. Also, a planar to cellular solidification mode transition is observed using SEM investigation. Finally, a yield strength of 800 MPa is recorded for the as-printed samples.

The second paper is written by Zopp *et al.* [5] and discusses the processing of Ti-5553

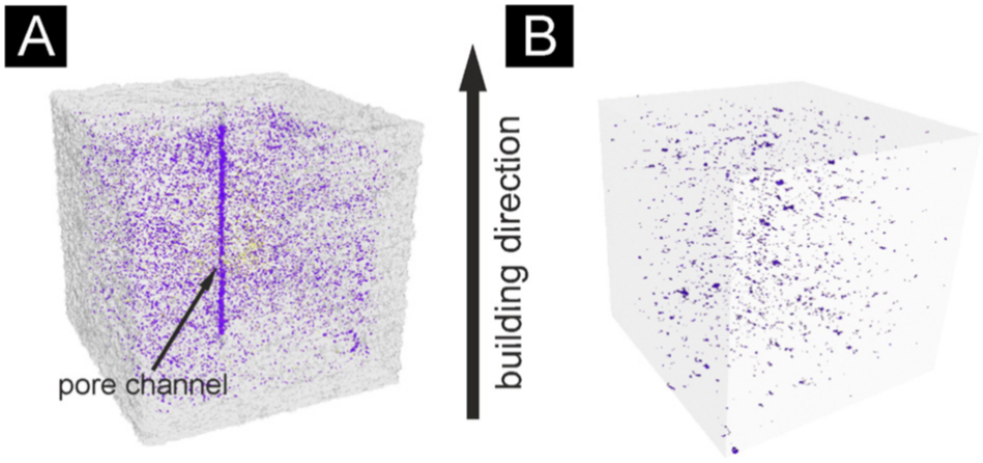

Figure 2.6: Nano-CT scan results showing (a) the sample with the hatching overlap of 60 µm and (b) the sample with the optimized hatching overlap of 120 µm [4].

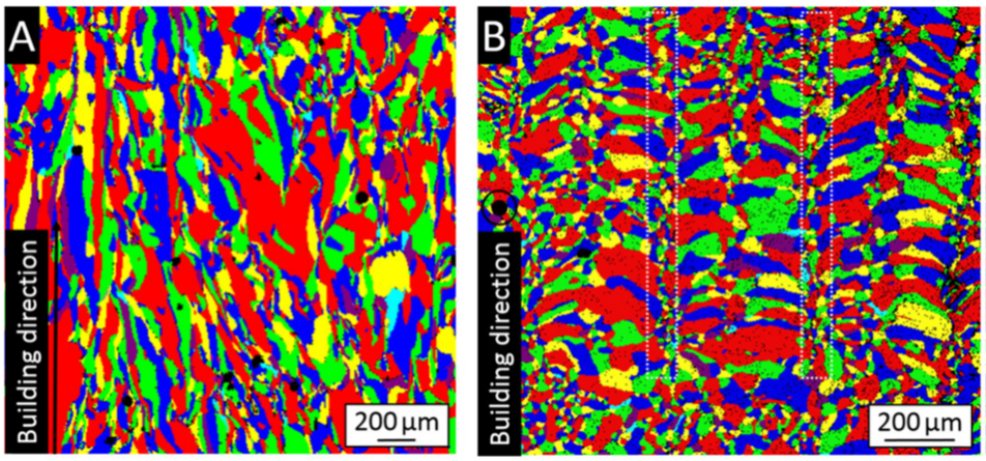

Figure 2.7: The EBSD results showing the texture in (a) the front cross-section and (b) the top view, respectively [4].

by continuous laser SLM. The research was done while the laser power and layer thickness were kept constant as 80 and 30 µm, respectively. The build plate was pre-heated up to 200 °C and the oxygen content was less than 0.10%.

Four main powder size ranges were tested, *i.e.* 25-32, 32-45, 45-53 and 53-63 µm. Even though a same heat input was applied to all of them, Figure 2.8 shows that by increasing the powder size, the surface roughness gets increases due to the presence of layer particles

stuck to the surface.

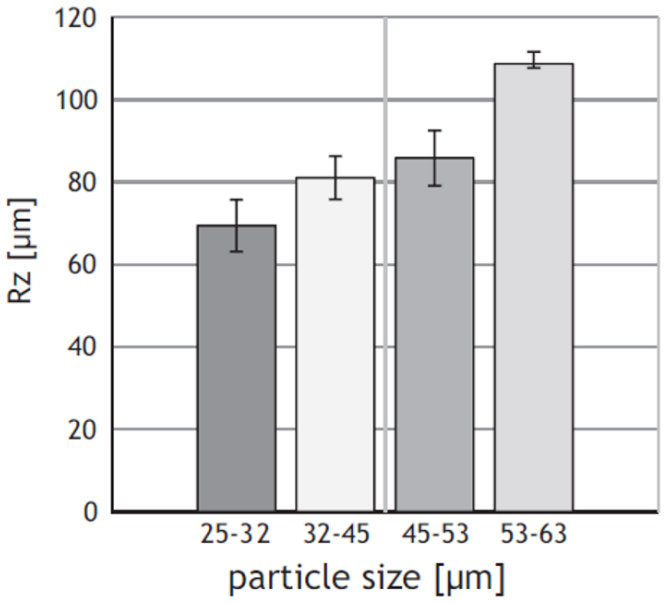

Figure 2.8: The surface roughness study results showing the effect of powder size range on the final roughness achieved [5].

The most recent article published regarding the SLM processing of Ti-5553 is also written by Shwab *et al.* [6]. In this paper, the possibility of in-situ heat treatment of Ti-5553 at the printing stage is investigated. To this end, the substrate was kept at 500 °C. The laser spot diameter used was 80 µm and the chessboard scanning strategy was utilized. Figure 2.9 clarifies the rationale of the research, which attempts to develop a method to avoid heat treatment after AM.

The XRD results shown in Figure 2.10 indicates that the samples printed on a pre-heated substrate had experienced an in-situ precipitation hardening treatment. In general, the volume fraction of α phase is zero, however, a 52% α fraction is reported for the hardened sample.

TEM results showed that the β to α transition was completed in the heat treated samples. Also, the tensile test results demonstrated a significant increase in the yield strength, *i.e.* from 800 to 1100 MPa, caused by the pre-heating of the substrate. Finally, the hardness increased from 290 to 463 HV when the heat treatment was done.

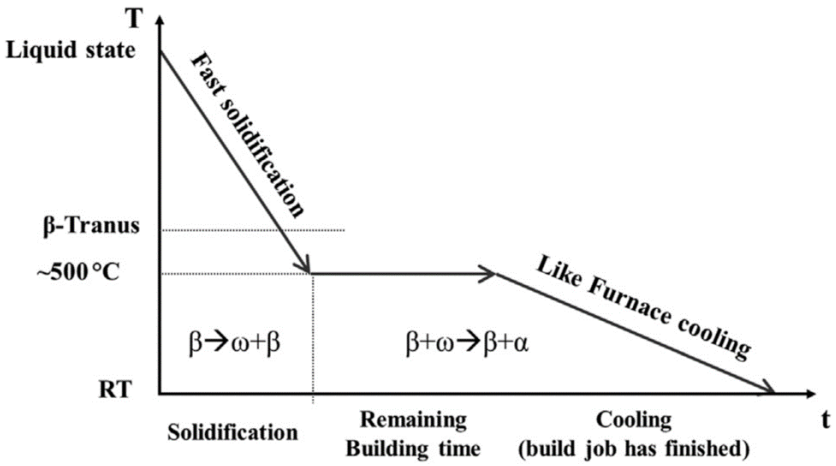

Figure 2.9: The heat treatment cycle used [6].

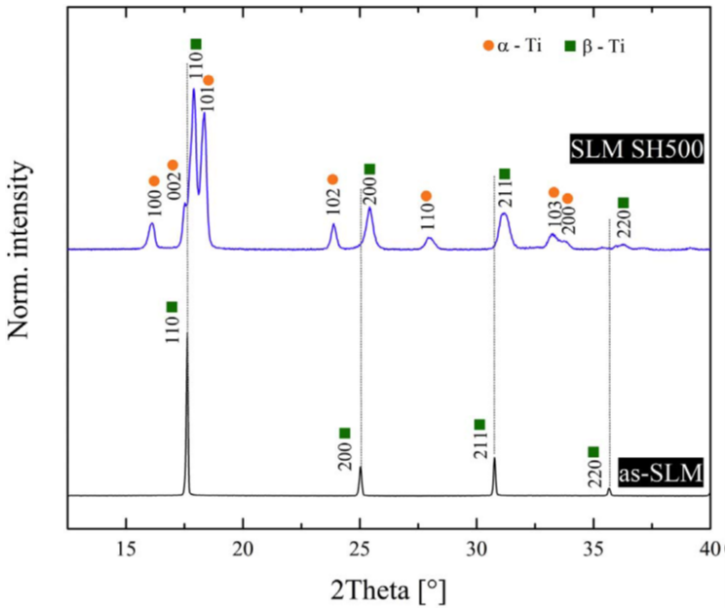

Figure 2.10: The effect of in-situ heat tratment on the α phase content of the printed samples [6].

Chapter 3

Experimental procedure

In this chapter, a brief review of the materials, equipment and methodology used is given. To this end, some important specifications of the as-received Ti-5553 powder as well as the processing and testing machines are first discussed. Afterwards, the experimental procedure is explained step by step.

3.1 Materials

3.1.1 Ti-5553 powder

The corresponding size distribution of the plasma atomized powder purchased is given in Table 3.1. One may see that the size range matches with that of 15-45 µm. The particle size distribution analysis was performed using a Coulter® LS particle size analyzer according to ASTM B822 [34].

Table 3.1: Particle size distribution analysis results

Cumulative mass	Diameter(µm)
D_{10}	22
D_{50}	35
D_{90}	46
<15 µm	3% by volume

In addition, Table 3.2 shows the results of the chemical analysis of the as-received powder confirming the Ti-5%Al-5%V-5%Mo-3%Cr composition of the alloy. The chemical analysis was performed using ASTM E1409 [35], ASTM E1941 [36] and ASTM E2371 [37] for the Oxygen and Nitrogen content, Carbon content and the metallic elements, respectively.

Table 3.2: Chemical composition of the virgin Ti-5553 powder

Element	wt.%
Al	5.14
V	4.98
Mo	4.97
Cr	2.91
Fe	0.37
O	0.09
N	0.01
C	0.01
Ti	Balance

3.1.2 Kroll's reagent

Kroll's reagent was used to etch the metallography samples. Table 3.3 shows the chemical composition of the etchant.

Table 3.3: The chemical composition of Kroll's reagent

Ingredient	Volume (ml)
Distilled water	92
Nitric acid	6
Hydrofluoric acid	2

3.2 Equipment

3.2.1 Renishaw SLM machine

A Renishaw AM 400 modulated laser and powder-bed fusion additive manufacturing machine shown in Figure 3.1 was used to investigate the printability of the Ti-5553 powder. The machine was equipped with a pulsed Ytterbium laser with the maximum power of 400 W and a large SafeChange™ filter. Three different scanning strategies were available: (I) Stripes, (II) Chessboard and (III) Total fill.

Figure 3.1: The modulated laser powder-bed additive manufacturing machine used [7].

The schematic illustration of each scanning strategy is shown in Figure 3.2. Each scanning strategy provides a number of advantages over the others, however, each has its own drawbacks. The pros and cons of each strategy is discussed previously in Chapter 2. Other scanning strategies like Meander are not used in this research.

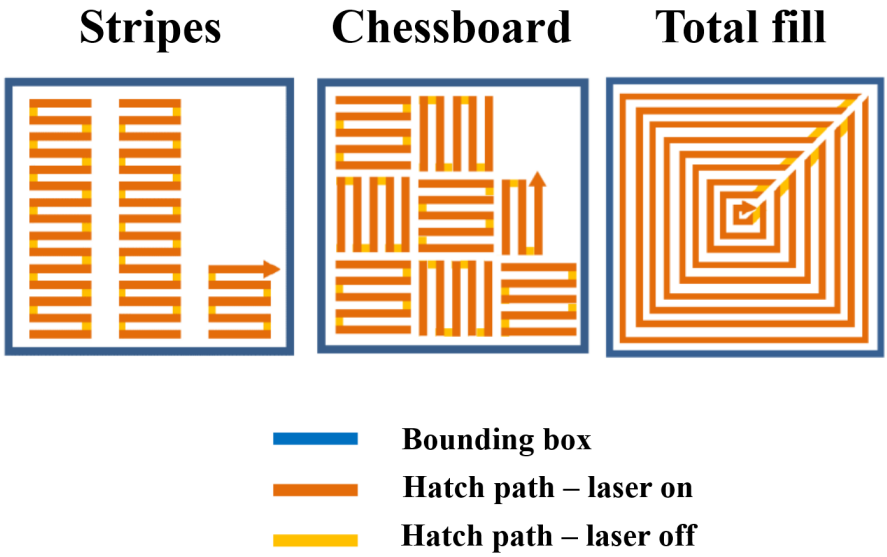

Figure 3.2: The different scanning strategies provided by the Renishaw machine.

3.2.2 ZEISS Nano-CT scanner

A ZEISS Xradia 520 Versa 3D X-ray Nano-CT scanner was used to investigate the porosity level of the samples. The resolutions of 0.5 and 12 µm per pixel were chosen to run the tests on the virgin powder and the printed samples, respectively. Also, Dragonfly™ software was utilized to analyze the scan results.

3.2.3 Keyence confocal microscope

A Keyence laser confocal microscope was used to study the surface profile and roughness of the printed samples. The microscope uses a UV laser and a 16-bit photo multiplier to accurately obtain measurement data from the samples and provides up to 500X magnification for microstructural investigations.

3.2.4 FT4 powder rheometer

The flow characteristics of the virgin powder was analyzed using a FT4 Powder Rheometer®. Properties like compressibility, permeability, shear, etc. can be assessed using this machine.

Each test was repeated three times on three different powder samples to minimize the errors.

3.2.5 ZEISS Ultra SEM

A ZEISS field emission SEM with the gun voltage of 20 kV was employed for microstructural investigations and to trace any phase formation or fine features that cannot be seen by OM. The secondary and backscattered electron modes were used for general observations and composition related studies, respectively. SEM/EDS was utilized for the chemical analysis.

3.2.6 JEOL 2010F TEM

TEM investigation was used to trace the phase transformation in each stage, *i.e.* the beta to omega and omega to alpha transformation. In addition, TEM/EDS was utilized to color map the alpha and beta stabilizer elements, separately. The operating voltage was set as 200keV. The samples were ground down to the thickness of 100 µm and then subjected to electro-polishing and ion-milling, performed respectively with Struers Twin-jet polisher and Gatan PIPS mill, around the hole made by electro-jetting.

3.2.7 Bruker D8 XRD machine

In order to characterize the virgin powder and the printed samples in terms of phase distribution, a Bruker D8 XRD machine with a Copper cathode was used. The working voltage was 40 kV and the current was 44 mA. The scan speed was selected as $0.5\,^{\circ}\,\mathrm{min}^{-1}$ and the scan range was set between 20-120°. The XRD sample preparation procedure will be discussed later in the methodology section.

3.2.8 CLEMEX CMT

The CLEMEX CMT automated micro-hardness machine was used to generate a color map of hardness variation in the printed samples. The force chosen was 300 gf and the dwelling time was set as 10 s. More than 1200 indents were made on each sample to insure the accuracy and coherency of the results, which were made at a 0.3×0.3 mm spacing on the cross-sectioned specimen after grinding and polishing.

3.3 Methodology

First, the powder characterization, in terms of rheometry, SEM, XRD and Nano-CT scan investigations, was done. In order to develop a printing recipe for Ti-5553, it was essential to first find the optimized VED. As there was no research found regarding the pulsed laser SLM of this alloy, the only practical approach was to use the data available for the continuous laser SLM of Ti-5553 and translate it for the Renishaw machine, as the start point.

Considering the paper by Schwab *et al.* [4] as the reference, a VED range of 92.6-388.0 J/mm^3 was first suggested. However, the range was expanded to 20.9-584.0 J/mm^3 so that the results would be more comprehensive. The major issue with the reference paper was the slow production rate, *i.e.* the very low scanning velocities and laser powers chosen. In order to turn the study into an industrialized process, it was decided to increase both the laser power and the velocity to maintain the new VED range and expedite the production rate, simultaneously.

To this end, three laser powers of 100, 187.5 and 275 W were selected. As described previously by Equation 2.4, point distance (p_d) and exposure time (e_t) are the two main parameters determining the scanning velocity of the pulsed laser SLM. To keep the VED in the specified range, a minimum, intermediate and maximum value was suggested for each of them, *i.e.* 30, 50 and 70 µm for the point distance and 46, 66 and 86 µs for the exposure time. Furthermore, the laser spot diameter and the layer thickness were set as 70 µm and 45 µm, respectively, and the chessboard scanning strategy was used for all of the experiments. An approximately 10 µs delay time may exist between each exposure cycle of the modulation procedure in Renshaw AM400. This delay was neglected in this study as it is still under investigation in consultation with the OEM. If validated, the VED values should be revised accordingly. This will be corrected/highlighted in our paper to be submitted shortly. Also the hatching distance and the overlap degree between each two chessboard patterns were kept constant as 95 µm and 20%, respectively.

Twenty-seven combinations were generated based on the three values considered for each variable. The list of process specifications is shown in Table 3.4. Two samples of A and B were printed for each combination to check the repeatability of the process. The samples were designed as cylinders with the diameter and height of 10 mm and 15 mm, respectively. Also, a cone was designed at the bottom of each sample so that it'd be easier to detach them from the build plate once the process was done. Three batches of 18 samples, *i.e.* 54 in total, were printed with the samples randomly distributed on the build plate to minimize the errors. Figure 3.3 shows the schematic illustration of a batch to be printed.

Table 3.4: List of parameters chosen to print the first batch of samples

Sample #	Power (W)	Exposure time (µs)	Point distance (µm)	Scanning velocity (m/s)	VED (J/mm^3)
1 AB	100	46	70	1.52	20.9
2 AB	100	46	50	1.08	40.9
3 AB	100	46	30	0.65	114.0
4 AB	100	66	70	1.06	29.9
5 AB	100	66	50	0.76	58.7
6 AB	100	66	30	0.45	163.0
7 AB	100	86	70	0.81	39.0
8 AB	100	86	50	0.58	76.4
9 AB	100	86	30	0.35	212.0
10 AB	187.5	46	70	1.52	39.1
11 AB	187.5	46	50	1.08	76.7
12 AB	187.5	46	30	0.65	213.0
13 AB	187.5	66	70	1.06	56.1
14 AB	187.5	66	50	0.76	110.0
15 AB	187.5	66	30	0.45	306.0
16 AB	187.5	86	70	0.81	73.1
17 AB	187.5	86	50	0.58	143.0
18 AB	187.5	86	30	0.35	398.0
19 AB	275	46	70	1.52	57.4
20 AB	275	46	50	1.08	112.0
21 AB	275	46	30	0.65	312.0
22 AB	275	66	70	1.06	82.3
23 AB	275	66	50	0.76	161.0
24 AB	275	66	30	0.45	448.0
25 AB	275	86	70	0.81	107.0
26 AB	275	86	50	0.58	210.0
27 AB	275	86	30	0.35	584.0

Once the samples were printed, they were first subjected to the Archimedes density analysis. To this end, the samples were each weighed three times in the wet and dried condition. The ideal density, *i.e.* the bulk with zero porosity level, of Ti-5553 was considered as 4.65 g/cm^3 [5]. The densities calculated by the Archimedes test were compared based on how close, in terms of percentage, they were to the ideal density. The surface roughness

of the samples were next evaluated by a Keyence confocal microscope, see Section 3.2.3 for more details. Afterwards, the Rockwell, *i.e.* HR_b and HR_c, test were used for hardness measurements. Five indents were made for each sample. The forces used was 150 kgf as suggested by the standards [38].

After the general tests mentioned were done, a few selected samples with the lowest, medium and highest densities were selected for a more detailed analysis. First, one sample from each category was subjected to Nano-CT scanning to determine their exact density. In addition, micro-hardness mapping was used to study the hardness distribution in the selected samples. Microstructural investigations in terms of OM, SEM and TEM were then carried out on 2 samples of each category. The details of the sample preparation procedure is shown in Table 3.5 which is basically the preparation suggested by Struers [39] with a slight modification. As mentioned before, Kroll's reagent was utilized to etch the samples and the etching time was 20 s. Finally, XRD analysis was used to compare the phase distribution before and after printing. The XRD samples were prepared by the coarse grinding procedure mentioned in Table 3.5.

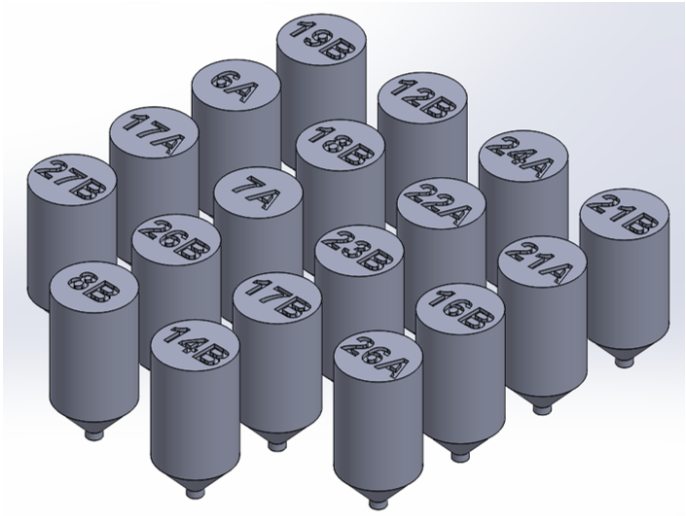

Figure 3.3: The input CAD file showing the random distribution of the samples on the first printing batch build plate.

Having determined the best VED in the first phase, the effects of geometry and scanning strategy on the final properties were studied next. Three different scanning strategies of stripes, chessboard and total fill were used to print the second batch. The details of each strategy is previously shown in Figure 3.2. All samples were printed with the same parameters used to print the sample #20 in the previous stage as it showed the best density

Table 3.5: The sample preparation procedure used for Ti-5553

Step	Coarse grinding	Fine grinding	Polishing
Surface	Sandpaper	MD-Largo	MD-Chem
Abrasive	SiC #320	Diamond 9 µm	Colloidal silica 0.04 µm
Suspension	Water	DiaPro 9	OP-S + 10%H_2O_2
RPM	300	150	150
Force (N)	Hand	30	30
Time (min)	Until plane	5	5

and mechanical properties. Also, two geometries of cylinder and cube, with the dimensions of D = 10 mm × H = 15 mm and 10 × 10 × 15 mm^3, respectively, were allocated to each scanning strategy.

Two identical samples of A and B were printed for each combination of geometry and scanning strategy leaving 12 samples printed in total. The specifications of each sample are listed in Table 3.6. The samples were distributed randomly on the build plate and a cone was designed at the bottom of each sample for easier detachment after printing. Figure 3.4 demonstrates the CAD design of the second printing phase.

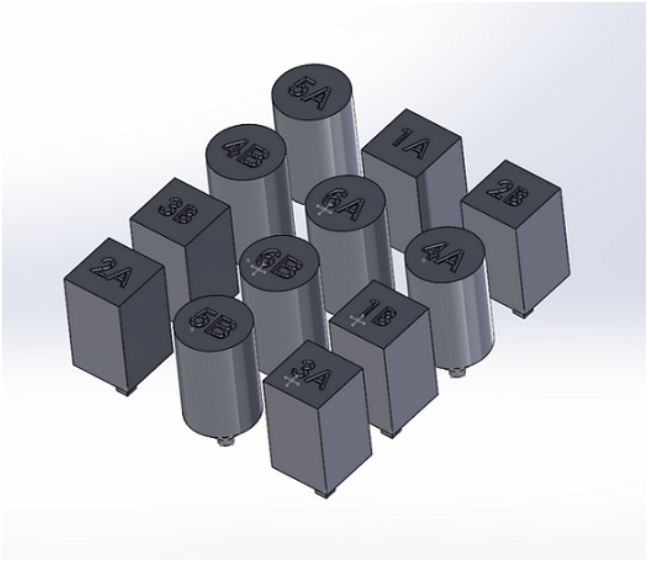

Figure 3.4: The input CAD file showing the random distribution of the samples on the second printing batch build plate.

Table 3.6: List of sample specifications for the second printing batch

Sample #	Geometry	Scanning strategy
1 AB	Cube	Stripes
2 AB	Cube	Chessboard
3 AB	Cube	Total fill
4 AB	Cylinder	Stripes
5 AB	Cylinder	Chessboard
6 AB	Cylinder	Total fill

After the printing stage, the samples were subjected to the Archimedes density analysis with the same procedure mentioned before. Then, the hardness measurement was performed using the HR_b and HR_c tests. One selected sample from each category of stripes, chessboard and total fill were next scanned by the Nano-CT scanner with the goal of having a more accurate density analysis and better comparison. Afterwards, the same samples were prepared as shown previously in Table 3.5 for the OM, SEM and EBSD observations.

Chapter 4

Selective laser melting of Ti-5553

In this chapter, a thorough discussion is given regarding the printability of Ti-5553 alloy. Starting with a thorough characterization of the powder, the chapter then explains the results of each printing phase in terms of density, surface roughness, hardness, OM, SEM, TEM, XRD and EBSD analyses to finally identify the best printing condition.

4.1 Powder characterization

The Ti-5553 powder purchased was characterized in terms of compressibility, permeability, size distribution, porosity level, chemical composition and microstructure. The powder rheometry results is shown in Figure 4.1. These results can be of high importance if one is planing to re-use the powder over and over since they provide a handful of data to optimize the life cycle of the powder [40]. After a few batches of printing, the rheometry of the virgin powder changes which directly affects the physical and mechanical properties of the printed part. Hence, it is advised to keep tracking the characteristics like compressibility and permeability after each batch. Powder processing, *e.g.* sieving, is needed for recylcling once a notable change in the rheometry results is seen. However, the recycled powder may not have the same quality of the virgin powder [41] and this causes various flaws in the powder, which adversely affects the mechanical properties of the printed part [42].

In order to verify the size distribution and sphericity of the virgin powder, SEM observation was used. Figure 4.2 shows a few images taken from the powder sample with different magnifications. It is seen that the particles are smooth and highly spherical which

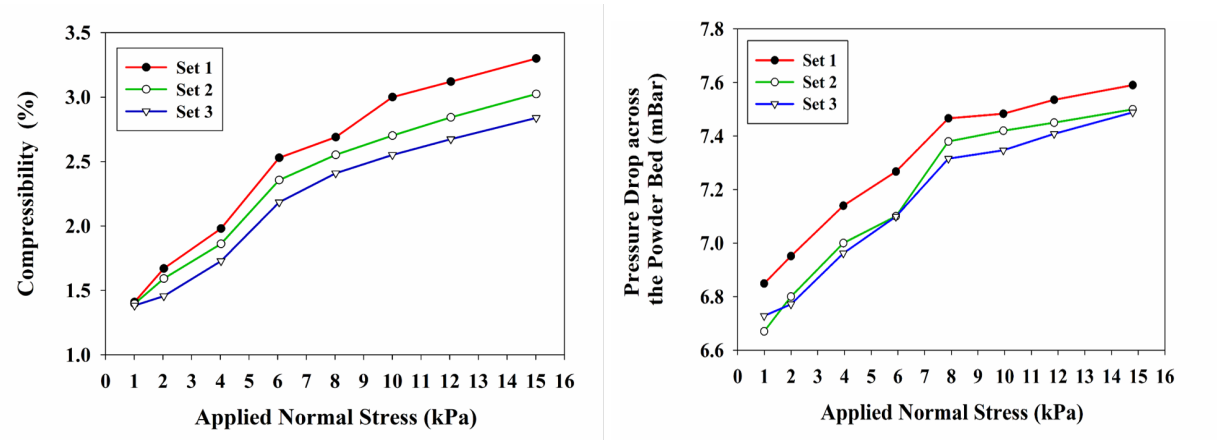

(a) (b)

Figure 4.1: The results for three repeat sets of samples showing (a) the compressibility and (b) the permeability of the as-received Ti-5553 powder.

indicates the good quality of it. Only a few non-spherical particles were detected by scanning the whole sample which is shown in Figure 4.3. Since the volume of such particles were less than 0.01%, their effect on the final properties is negligible.

Image analysis technique was used to check the size distribution of the powder. To this end, 20 SEM images were use to measure the diameter and sphericity factor of each particle. The results proved that although it was first assumed that the powder size range is between 15-45 µm, there are numerous fine particles with the diameters of below 10 µm.

The reason is that such small particles are, in most of the cases, electro-statically bonded or fused partially to the surface of larger particles. That results in a cluster of large particles with smaller ones fused in between. The majority of industrialized size distribution analyzer machines use a shadowing system which is basically a light source emitting as the powder particles are falling from a vibrating channel leaving their shadow on a white background behind them which is being detected by a built-in camera. The process is faster compared to the image analysis but it cannot distinguish individual particles that are partially fused together to form a cluster. Hence, the range given by the powder supplier, *i.e.* 15-45 µm, is relatively high due to the fact that the machine fails to detect finer particles. Figure 4.4 demonstrates ultra-fine particles at the interface between two large ones.

A combination of large and fine powder particles is suitable for powder-bed fusion system as the finer particles fill the gap in between the larger ones leading to higher density, *i.e.* porosity level, of the printed part. In addition, spherical powder shape and

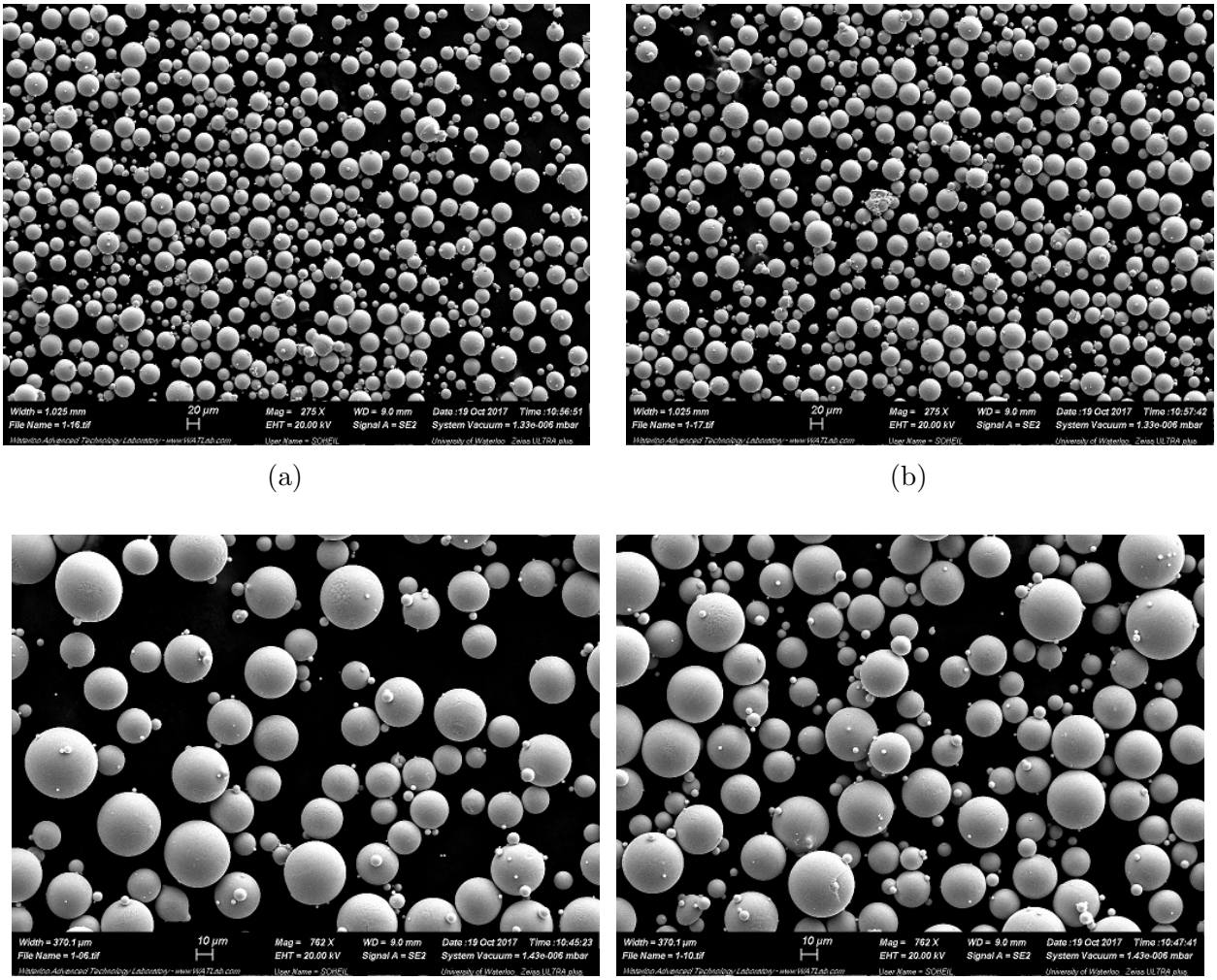

(a) (b)

(c) (d)

Figure 4.2: SEM images taken from the virgin powder using low (a and b) and high (c and d) magnifications.

high packing density ensures good flowability which is crucial while powder-bed fusion systems are employed.

Figure 4.5 illustrates the image analysis results. It is observed that about 70% of the detected particles are finer than 10 µm in diameter. In addition, about 95% of the particles had a sphericity factor of more than 0.98, where a sphericity factor of 1.00 represents a perfect sphere, which confirms the good quality of the powder. The details of this analysis

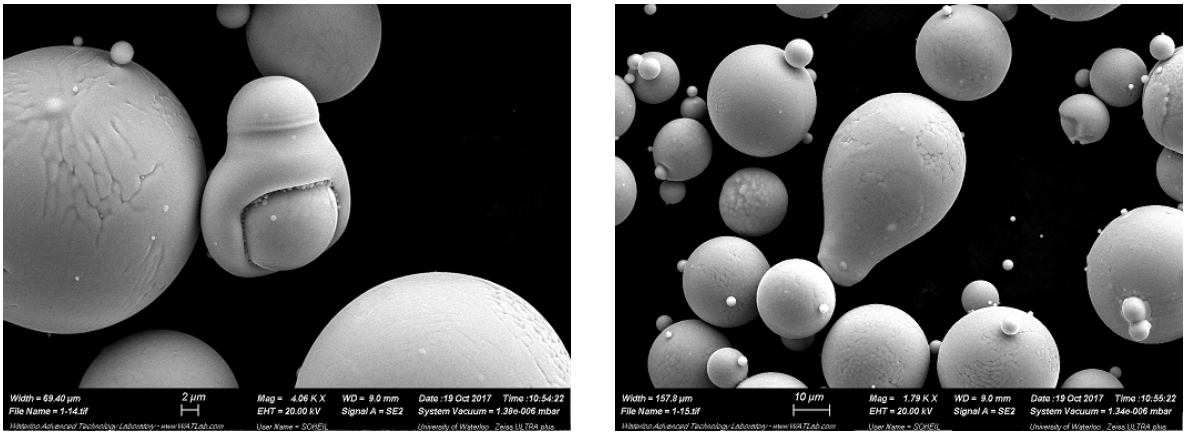

(a) (b)

Figure 4.3: Two examples of the non-spherical particles observed.

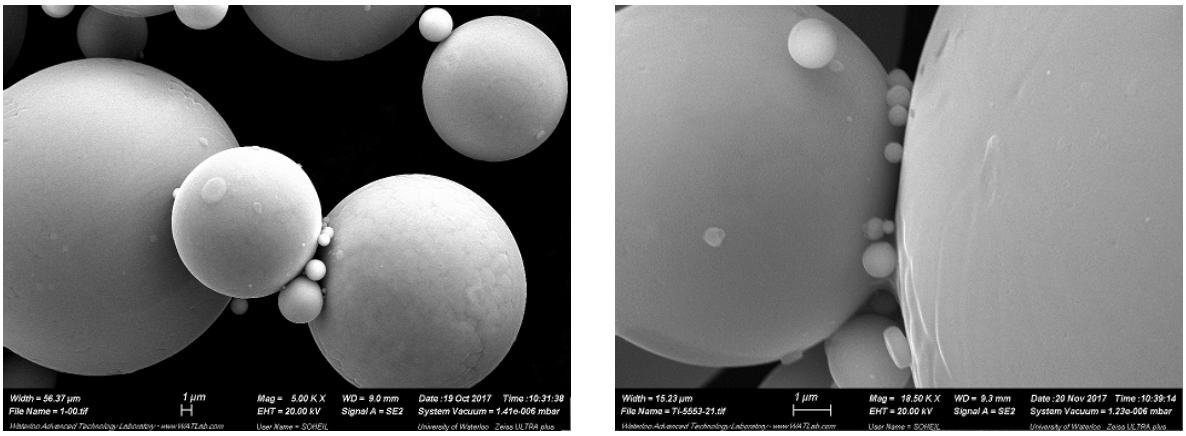

(a) (b)

Figure 4.4: Ultra-fine particles partially fused to the interface of larger ones.

is shown in Table 4.1. It is seen that the powder size ranges from 0.4-52 µm while the mean sphericity of the particles is 0.96. The EDS results shown in Table 4.2 confirm the Ti-5%Al-5%V-5%Mo-3%Cr composition of the alloy.

In order to do a preliminary analysis on the internal porosity level of the particles, a powder sample was mounted in Bakelite. The sample was next ground and polished following the preparation procedure presented in Chapter 3 Figure 4.6 demonstrates the SEM images taken from the sample. It is seen that the particles possess a high density

as no pits or holes were detected inside them. The microstructure suggests a dendritic solidification for the powder which is common due to the very high cooling rate associated with the plasma atomization process. The contrast between the crust and interior of the particles can be a result of surface oxidation or phase difference which will be clarified further when discussing the XRD results.

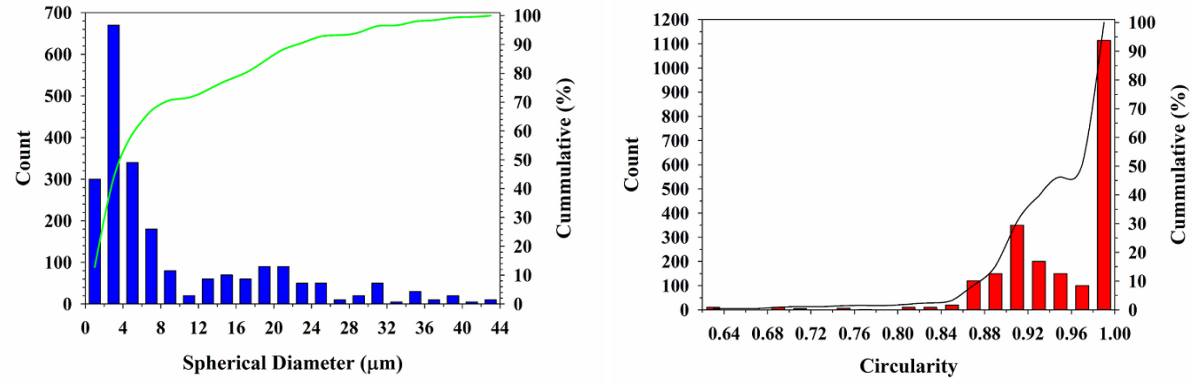

(a) (b)

Figure 4.5: The image analysis results showing (a) the size distribution and (b) the sphericity of the powder particles.

Table 4.1: The summary of the image analysis results

Analysis	Count(#)	Minimum	Maximum	Average	Standard deviation
Size distribution	2237	0.48 µm	52.85 µm	12.36 µm	12.48 µm
Sphericity	2237	0.62	1.00	0.96	0.05

Table 4.2: The EDS analysis results done on the powder sample

Element	wt.%	Error
Al	5.48	7.99
V	5.06	7.09
Mo	4.18	9.69
Cr	2.64	8.18
Ti	Balance	-

Figure 4.7a shows the powder sample scanned by the Nano-CT scanner. One may note particles with different sizes and random distribution indicating a proper sample extraction. As illustrated in Figure 4.7b, only two pores were detected inside the particles which confirms the SEM observation results.

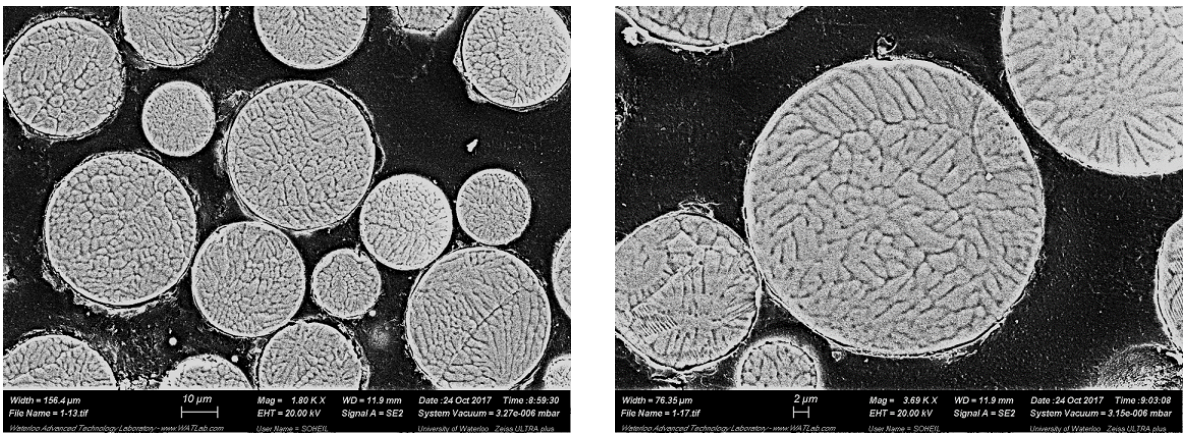

(a) (b)

Figure 4.6: The SEM observations revealing inside of the particles.

Since the alloy is considered a near beta composition and the plasma atomizing imposes very high cooling rates, the powder is expected to consist of pure beta phase, however, the XRD results demonstrated in Figure 4.8 reveals that the virgin powder has a small portion of alpha phase. This matter can be explained by the fact that, as described before in Table 3.2, there is about 0.1% Oxygen in the as-received powder.

Oxygen is an alpha stabilizer and is more likely to be found at the surface of the particles due to surface oxidation. In addition, Titanium has a high tendency to react with Oxygen even in room temperature and form a passive layer of oxide which explains the reason for the contrast between the crust and the interior of the particles. The results suggest about 17.7% alpha to be present in the virgin powder, however it should be noted that the X-rays only penetrate a few microns into the particle surface where most of the Oxygen contamination could be expected. This data can be used to compare the phases before and after printing the samples and helps to discuss the microstructural evolution.

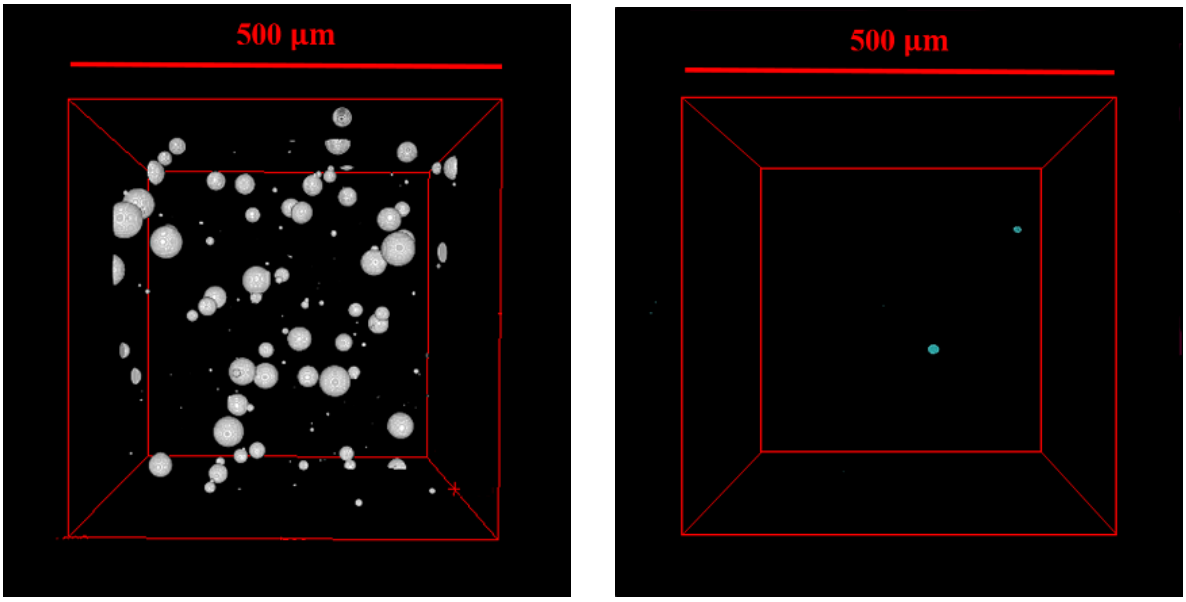

(a) (b)

Figure 4.7: The Nano-CT scan test results showing (a) the powder particles and (b) their internal pores.

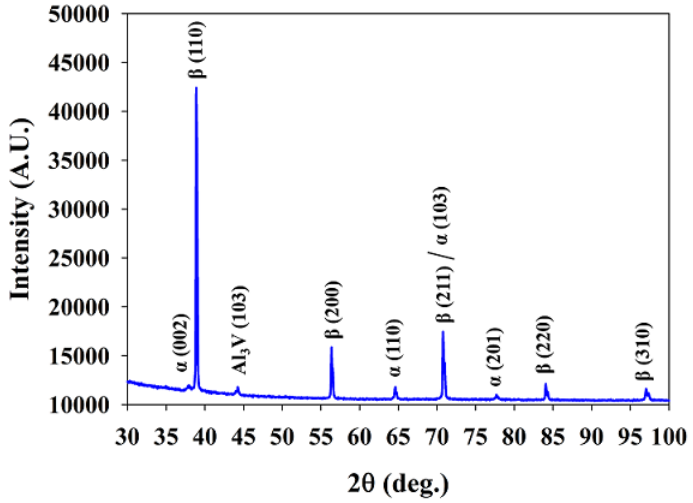

Figure 4.8: The XRD results performed on the virgin powder.

4.2 Effect of volumetric energy density

In the first phase of the research, effect of VED on the density, hardness, surface roughness and microstructure of the printed samples was investigated. A total of 54 samples, *i.e.* 2 samples of A and B for each condition, were printed which the specifications shown previously in Table 3.4. Figure 4.9a shows a printed batch of samples in phase 1. One may note that the samples are randomly distributed on the build plate. It was found that the samples printed with high VEDs had an oxidized surface due to the high heat input applied especially at the cone-shaped end which was a constricted path for heat flow. Figure 4.9b shows the oxidized surface while printing of sample #27 which had a VED of 584 J/mm^3.

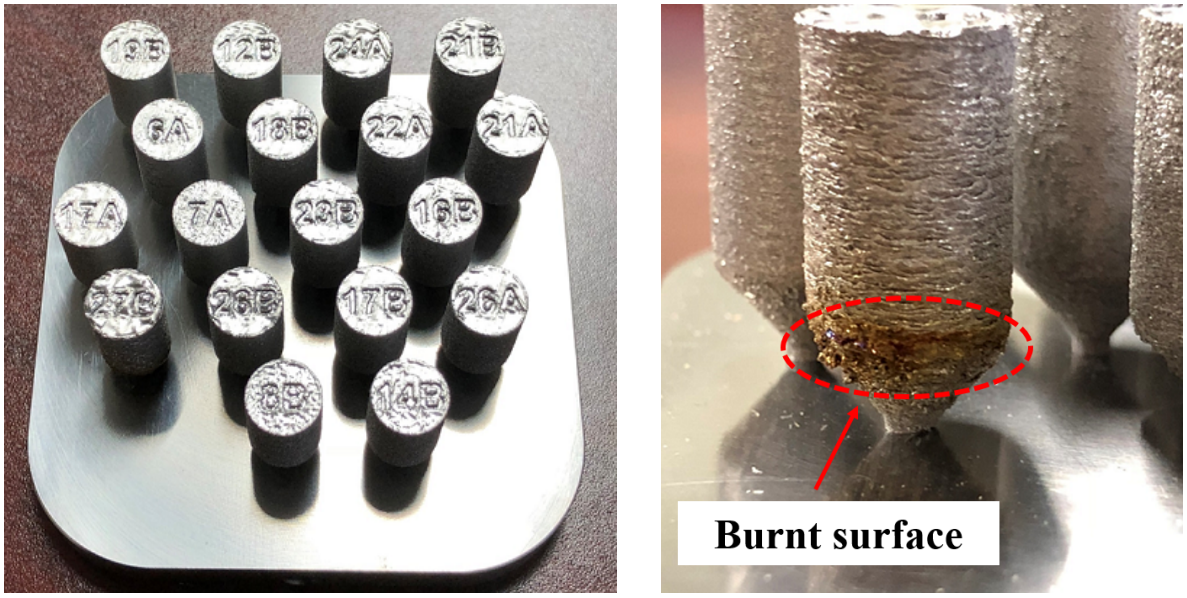

(a) (b)

Figure 4.9: The as-printed batch showing (a) the random distribution of the samples and (b) the burned surface of the sample with high VED.

By performing the Archimedes density analysis, it was observed that about one-third of the samples showed a relative density of more than 99.5%. Figure 4.10 shows the relative density vs. VED while the relative density of 1.00 represents the ideal density. It is clear that most of the samples with high relative densities have a VED range of 50-175 J/mm^3. Amongst them, samples #20, 22 and 11, *i.e.* VEDs of 112.0, 82.3 and 76.7 J/mm^3, exhibit the best relative densities of 99.92%, 99.87% and 99.80%, respectively.

In addition, the specimens with the highest VEDs exhibit an intermediate density. For instance, samples #27, 24 and 18 with the VEDs of 584.0, 448.0 and 398.0 J/mm^3 have relative densities of 96.72%, 98.35% and 96.81%, respectively. On the other hand, the samples with the lowest VEDs like 20.9, 40.9 and 29.9 J/mm^3, *i.e.* samples #1, 2 and 4, exhibit the lowest relative densities of 91.01%, 93.53% and 95.14%, respectively.

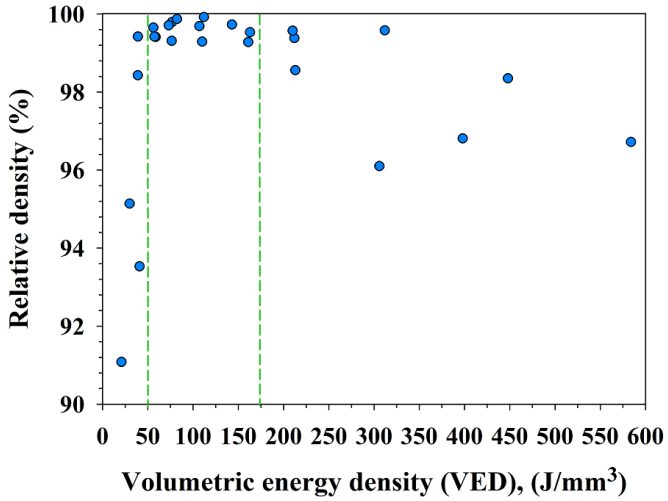

Figure 4.10: Effect of VED on relative density of fabricated Ti-5553 specimens.

Figure 4.11 shows the results of analysis done on the density measurement data. It is evident that there is an optimum heat input range, which is governed by the laser power and scanning velocity, leading to higher density. As demonstrated in Figures 4.11a and 4.11b, a combination of low laser power and high scanning velocity results in a poor density as a consequence of low heat input. This matter can cause lack of fusion which, in turn, contributes to internal porosity level [43]. On the other hand, a combination of high laser power and low scanning velocity leads to spattering and gas absorption due to the excess heat input applied [43]. Consequently, a higher porosity level is observed for such combinations.

As described in Equation 2.4, the scanning velocity in a pulsed laser system is governed by the point distance and exposure time. Figures 4.11c and 4.11d highlight the effect of these parameters on the final density attained. One may see that a combination of wide point distance and low laser power leads to a poor density. In fact, the wider the point distance is, the higher the scanning velocity will be. As a consequence, the amount of heat input decreases by increasing the point distance resulting in the lack of fusion. On

the other hand, spattering occurs by applying a high laser power and using a short point distance due to excessive heat input.

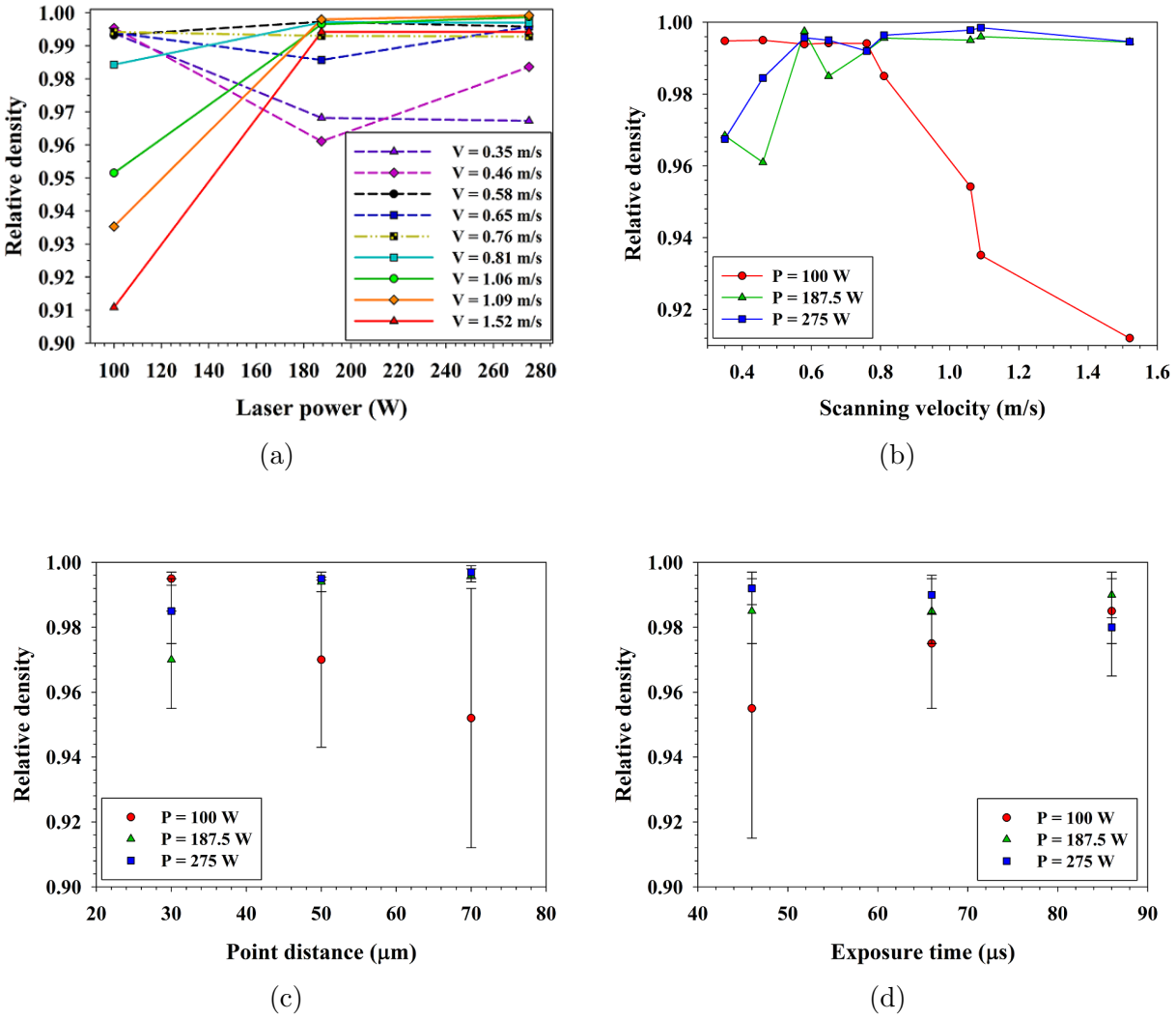

Figure 4.11: The Archimedes density analysis results showing the effect of (a) laser power, (b) scanning velocity, (c) point distance and (d) exposure time on the relative density achieved.

Similarly, it is observed that the porosity level increases by applying a very long exposure time. Longer exposure times for each laser shot means slower scanning velocity, and

in turn, higher heat input. On the contrary, a short exposure time coupled with a low laser power leads to the lack of fusion due to insufficient heat input.

In order to compare the samples with a higher accuracy, samples #20 and 27, *i.e.* the best and highest VEDs respectively with 112.0 and 584.0 J/mm^3, were selected for

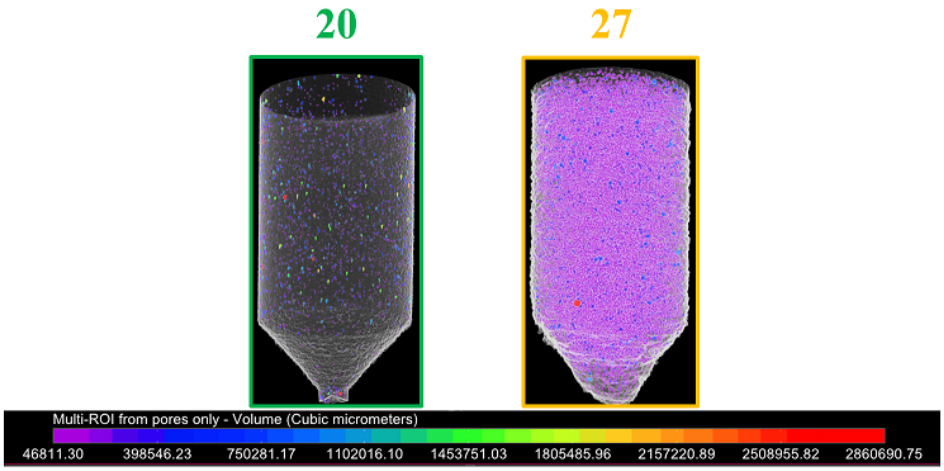

(a)

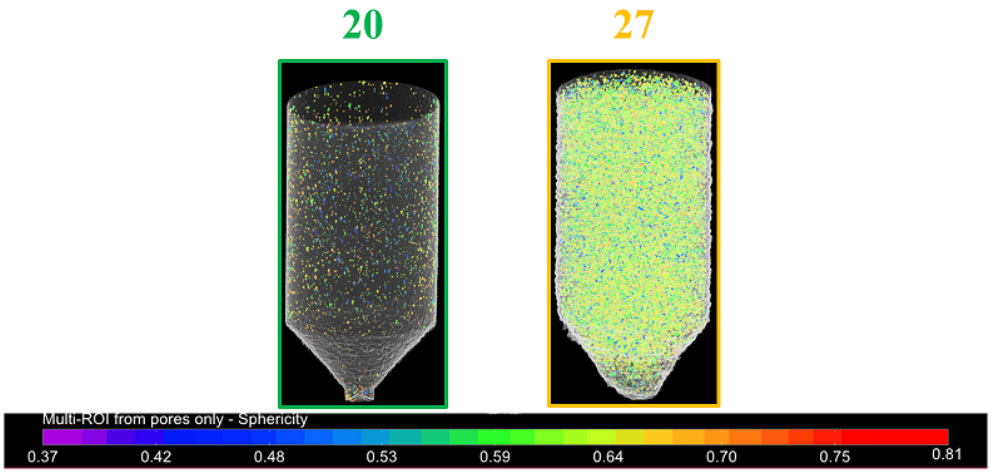

(b)

Figure 4.12: The Nano-CT scan results showing (a) the size distribution and (b) morphology of the internal porosities for the samples with the best and highest VEDs used.

Nano-CT scanning test. Figure 4.12 illustrates the distribution of internal porosities and their sphericity for each of the samples. In addition, a quantitative analysis regarding the porosity level is given in Figure 4.13a. It is observed that there is a wide range of pore sizes detected in both samples most of which are in the range of 0.05×10^6 - 1×10^6 µm^3. It is also seen that the number of pores inside the sample printed with the highest VED is much higher. Furthermore, numerous pores larger than 1×10^6 µm^3 were found inside the sample 27.

Moreover, Figure 4.13b illustrates the sphericity of internal pores detected. One may see that most of the pores in both samples have a sphericity factor of 0.4 - 0.8 where the factor of 1 represents a perfect sphere. Hence, it can be concluded that the pores are somewhat spherical, *i.e.* neither bar-shaped nor completely spherical.

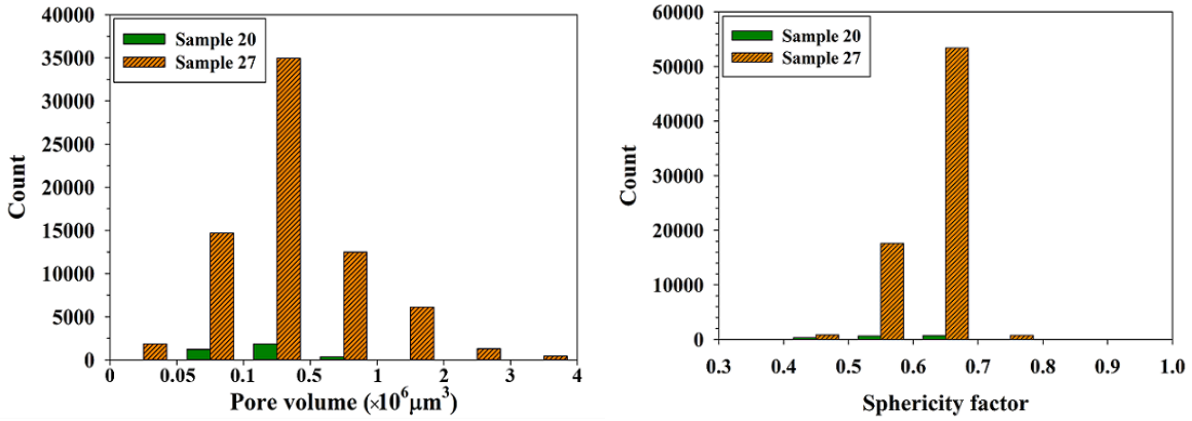

(a) (b)

Figure 4.13: The quantitative Nano-CT scan results showing (a) the pore size distribution and (b) the sphericity of them.

Figure 4.14 demonstrates the average surface roughness reported for each printing condition. The area between the green vertical lines represents the pre-determined VED range resulting in the best densities achieved, see Figure 4.10. However, one may notice a significant variation of surface roughness within that range. Even by considering two samples with a very similar VED values, the surface roughness is different because it is not strongly dependant on the VED.

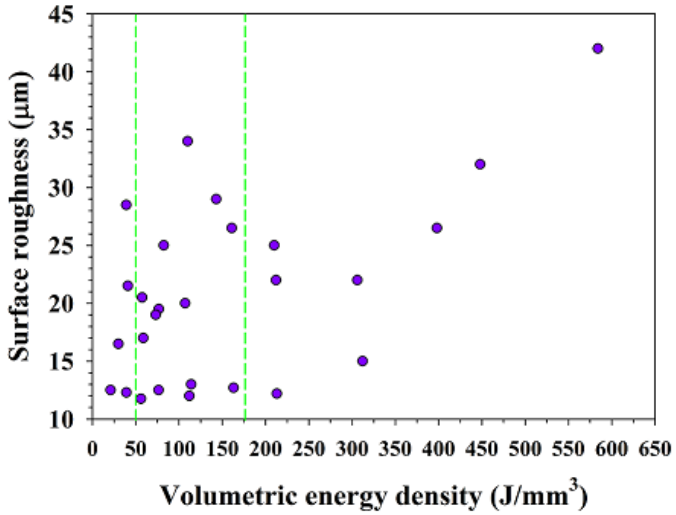

Figure 4.14: Effect of VED on the surface roughness of the printed samples.

Although two samples may have a similar VED, they do not necessarily have the same process parameters, *i.e.* the laser power, point distance and exposure time. By analyzing the color map given in Figure 4.15a, it can be concluded that while applying a rather low laser power, a combination of high exposure time and high point distance is not suitable. As the laser power increases, see Figure 4.15b, one should increase the point distance and keep the exposure time as short as possible to achieve the desired roughness. As shown in Figure 4.15c, exposure time is the dominant factor determining the surface quality of the printed sample while a high laser power is chosen. A short exposure time coupled with a medium point distance is found to provide the best results in this case.

Table 4.3 shows the hardness test results done on three selected samples from each category of low, best and high VED range. Samples #1, 2 and 4 represent, respectively, the three lowest VEDs while samples #27, 24 and 18 are the highest VEDs tested, accordingly. Finally, samples #20, 22 and 11 are the three highest densities achieved.

It is observed that the samples in the "low VED" category were so soft that their hardness numbers recorded were in the range of HR_b. The samples with the best densities had a hardness number of about 26 HR_c which is comparable to the hardness of a pure beta phase [44]. On the other hand, an average hardness of about 41 HR_c was recorded for the "high VED" category which is almost comparable to a homogenized and aged Ti-5553 [45]. This hardness is a sign of the in-situ heat treatment, *e.g.* precipitation hardening, in high

VED samples during the printing phase. The in-situ precipitation hardening phenomenon is frequently reposted by other researchers especially while applying high heat inputs or keeping the substrate in a specific temperature [46]. However, the precipitation might not take place homogeneously within the printed sample as the bottom, *i.e.* first printed, layers experience much more re-heating cycles compared to the top, *i.e.* last printed, layers. Thus, the aging treatment is more likely to occur at the bottom section of the samples.

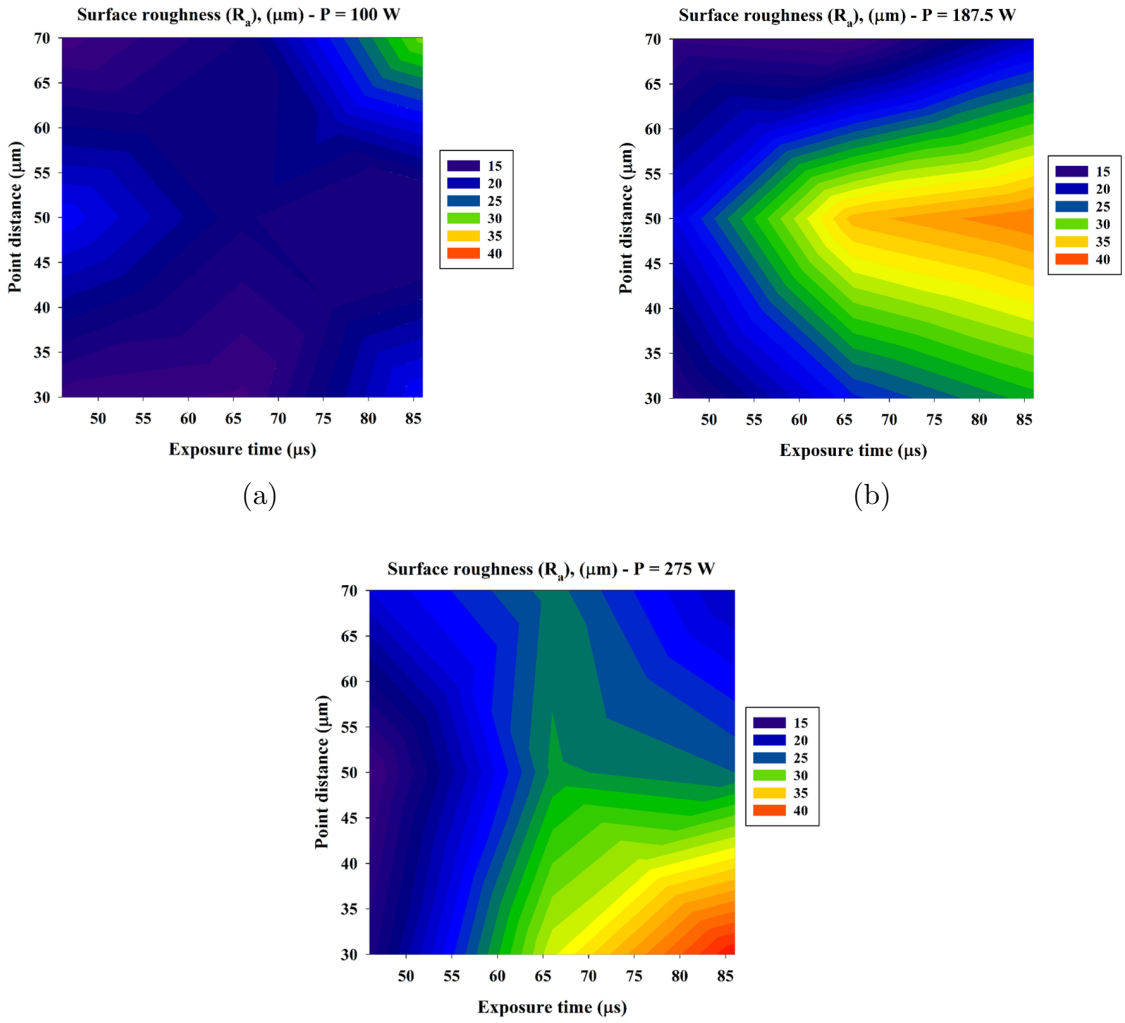

Figure 4.15: The color map contours showing the effect of exposure time and point distance on surface roughness while using different laser powers.

Table 4.3: The Rockwell hardness test results performed on the low, best and high VED samples

Category	Sample #	Test method	Hardness number
Low VED	1A	HR_b	50
	2B		85
	4A		91
Best VED	11A	HR_c	26
	20A		26
	22B		27
High VED	18A	HR_c	42
	24B		41
	27A		38

Figure 4.16 illustrates the XRD results. One can note that the sample 20, *i.e.* the best density, consists of a pure beta phase while the sample 27, *i.e.* the highest VED, relatively appears to contain significant fraction of α phase. As discussed before, the high heat input applied to the sample 27 facilitates the in-situ heat treatment of the sample being printed.

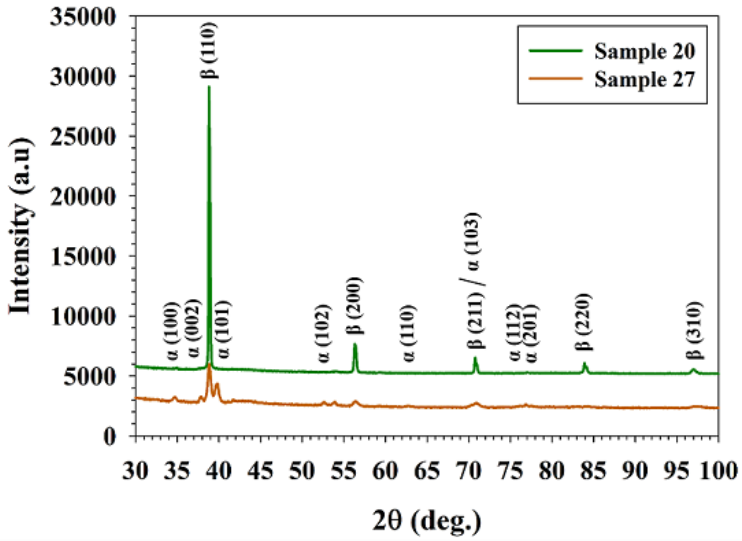

Figure 4.16: The XRD results comparing the samples with the best and the highest VEDs.

Figures 4.17 shows stereo microscopy images taken from the selected samples in front view. The notches at the top of each samples are an artifact of the printed sample codes. One may see a very high porosity level in the low VED samples, even though they show a rather smooth surface roughness. Although the number and size of the pores decrease in the high VED samples, yet the surface roughness has been deteriorated and the samples are not dense enough. Finally, the samples in the optimized VED range not only have the best density but also the smoothest surface roughness.

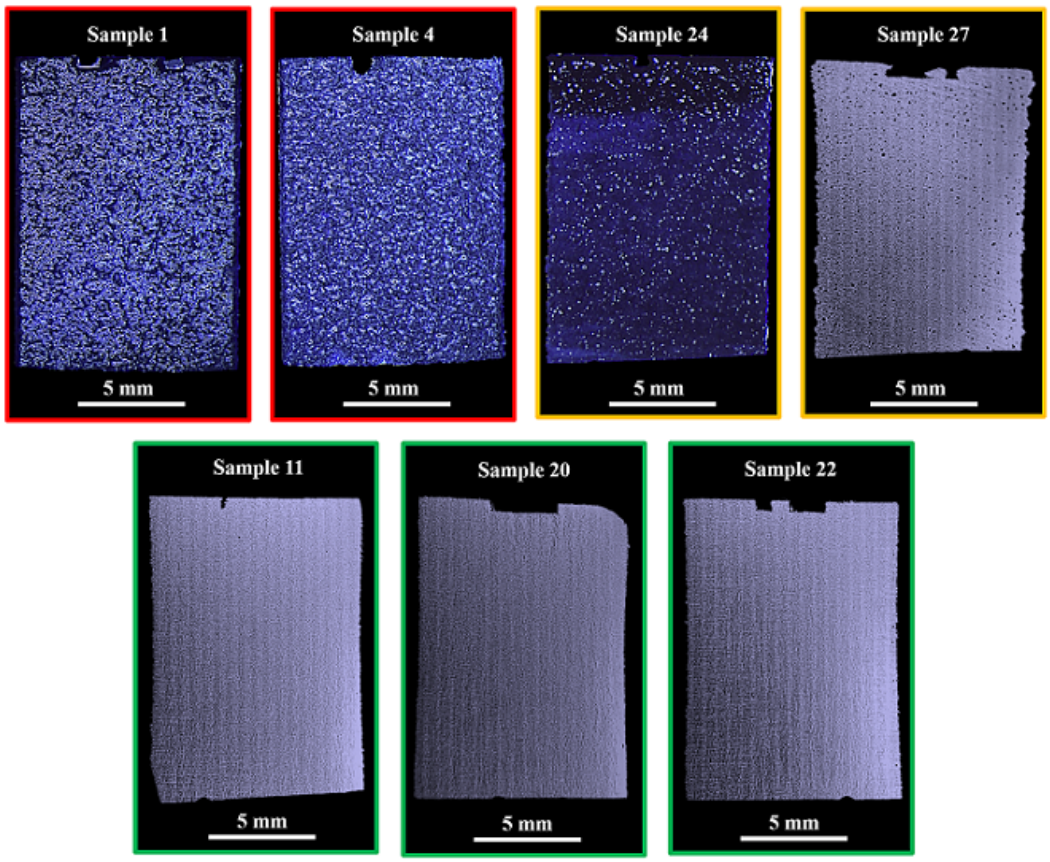

Figure 4.17: The stereo microscopy images showing the porosity level and surface condition of the printed samples sectioned along their diameter.

In addition, Figure 4.18 demonstrates the top view stereo images taken from the samples. The same trend is seen clearly in terms of the low VED samples representing the worst density and medium roughness while the high VED samples show a slightly better density but their surface roughness is not suitable. On the other hand, the best density

and roughness is observed in the optimized VED samples.

The laser track lines are clearly seen in the optimized VED samples showing the chessboard scanning strategy. However, as it is very difficult to grind the samples with zero tilt angle, the current images are showing several printing layers meeting each other. Based on the thickness measurements, a variation of about 100 µm is observed which explains the presence of 3 layers in the images considering the layer thickness was kept constant at 45 µm.

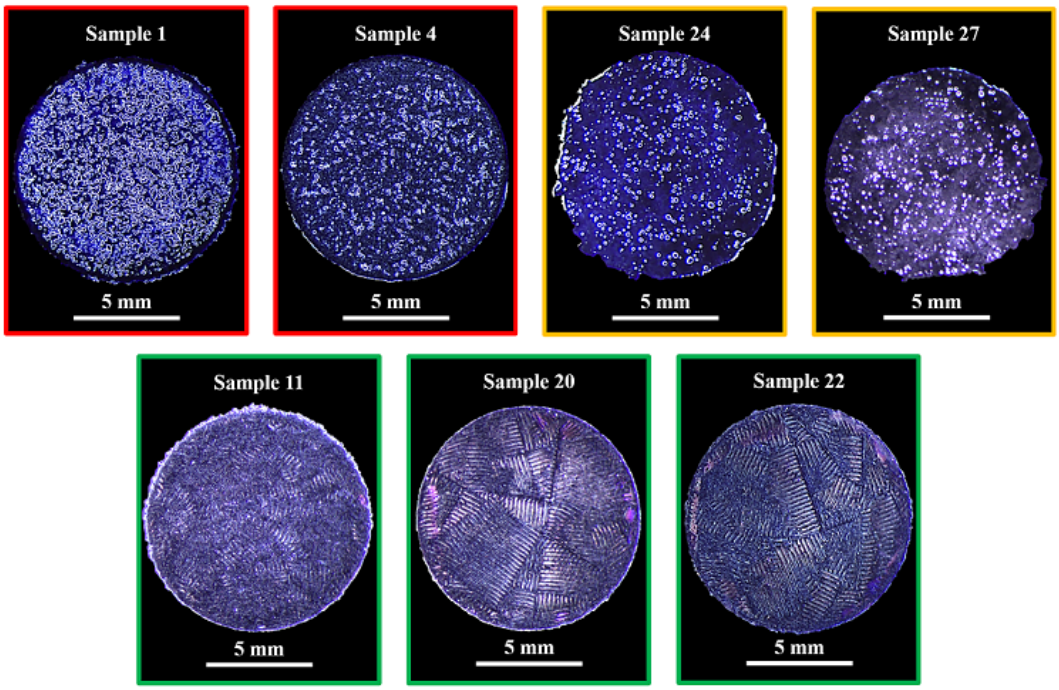

Figure 4.18: The stereo microscopy images showing the porosity level and surface condition of the printed samples in top view.

In order to check the hardness homogeneity in each category, two Vicker's microhardness color maps are given in Figure 4.19. A homogeneous hardness distribution is observed in sample 20, see Figure 4.19a. The decrease in hardness is evident as the blue areas, and attributed to the presence of the notches at the top and, potentially, the internal porosities nearby. In addition, one may note a slight banding pattern occurred due to the scanning pattern, however, the hardness variation is less than 10 Vickers in most of the cases, and the sample shows a promising hardness average of around HV 290.

On the other hand, the hardness map shown in Figure 4.19b reveals an inhomogeneous

hardness distribution for sample 27. While the fraction of blue areas corresponds to the high internal porosity level, and one may notice that there is a gradual hardness transition along the building direction from the top to the bottom of the sample. By comparing the two samples, it can be seen that the top part, *i.e.* the last layers printed, of sample 27 shows almost the same hardness value measured in sample 20. However, by tracking the hardness towards the bottom of the sample, the hardness increases significantly to around HV 500 which is comparable to peak aged Ti-5553 [45]. The reason can be attributed to the fact that the bottom layers experience frequent re-heating cycles which provides the activation energy required for the nucleation and growth of the alpha precipitates inside the beta matrix. This theory will be assessed later where the microstructures are characterized.

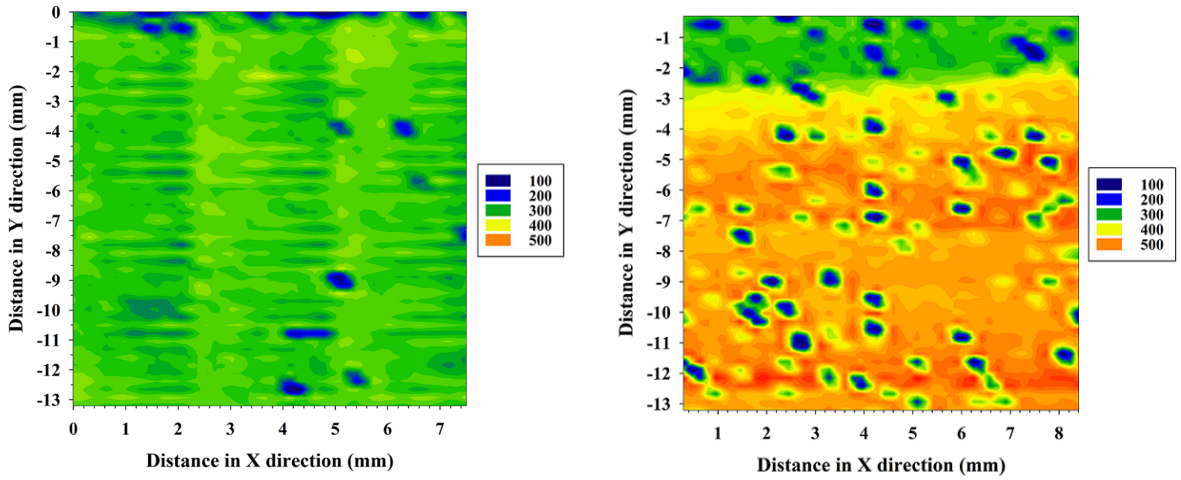

(a) (b)

Figure 4.19: The micro-hardness color maps showing (a) sample 20 and (b) sample 27 at the front view.

Figure 4.20 illustrates the cross-section along the diameter, *i.e.* the front view, OM images taken from samples# 1, 20 and 27 as the lowest, best and highest VEDs, respectively. The porosity observed in the low VED sample are not spherical indicating the process-induced defects due to lack of scan path overlap [47]. The pore sizes are found to be much larger than the other two samples and the lack of fusion in terms of layer inconsistency is evident. The high VED sample, on the other hand, has more spherical shaped pores as a consequence of gas-induced defects [48, 49]. These kinds of pores occur as a result of spattering which increases the chance of gas absorbtion.

The columnar growth of grains is more clearly seen in the best density sample compared

to the other two. One may see that that the grains are aligned with the building direction, *i.e.* vertically, forming a highly textured part. Some of the grains are as wide as 100 µm. This columnar texture is common in the as-printed samples, and happens due to epitaxial growth of the previously printed layers while printing a new layer on top of them [50, 51, 52, 53]. In fact, the grains follow the heat path which, in this case, is vertical. Although some pores can be detected, this sample is clearly much denser.

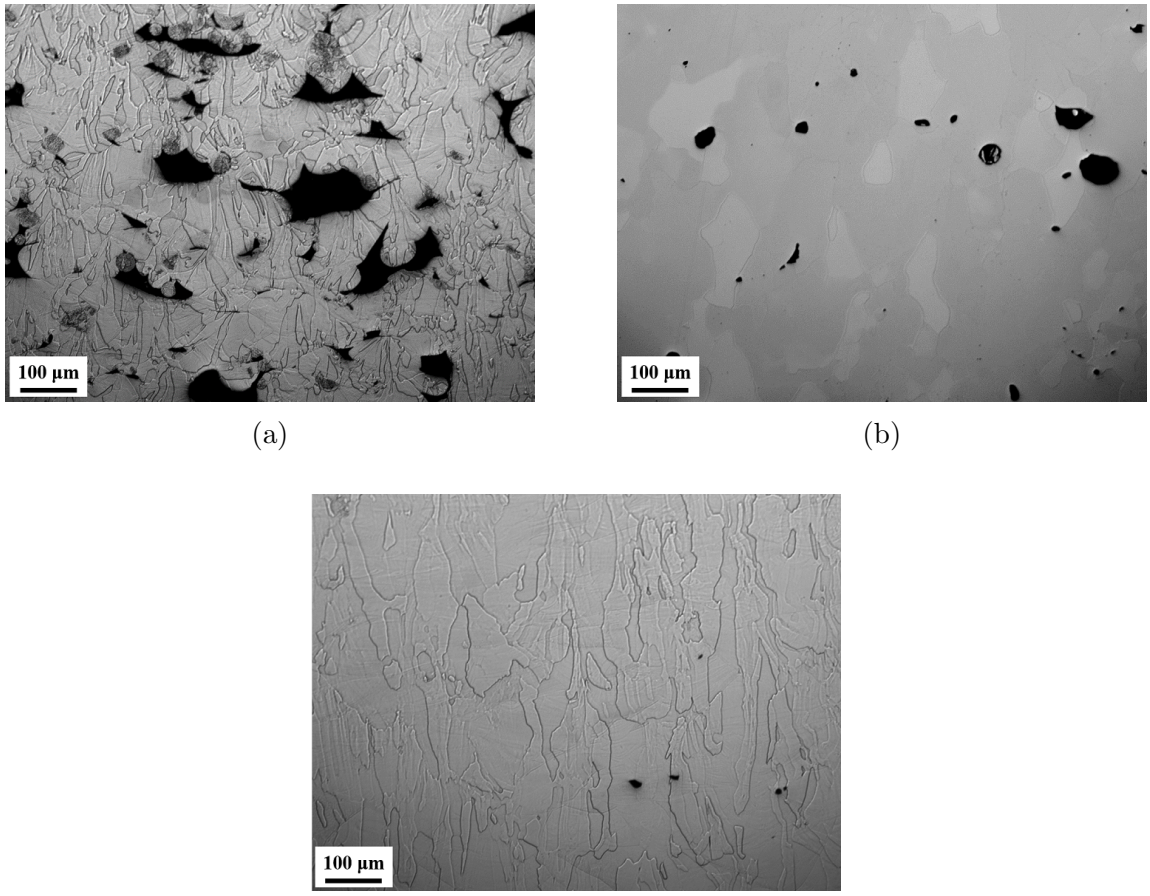

(a) (b)

(c)

Figure 4.20: The front view OM images showing (a) the lowest VED, (b) the highest VED and (c) the best density samples, respectively.

Figure 4.21 shows the top view, *i.e.* the last layer printed, optical microscopy images taken from the lowest, highest, and best VED samples. One may notice a similar trend in terms of the lack of fusion phenomenon occurred in the low VED sample and the spherical

porosities detected in the high VED sample. In addition, the laser scanning tracks are clearly seen in the best density sample. The width of the vertical bands perfectly matches with the laser spot diameter which was kept constant as 70 µm. It is observed that finer grains are formed at the interface between the tracks while coarser ones are detected inside each track. Moreover, very fine features are observed inside the high VED sample which are suspected to be the alpha precipitates. This theory will be confirmed later while discussing the SEM and TEM results.

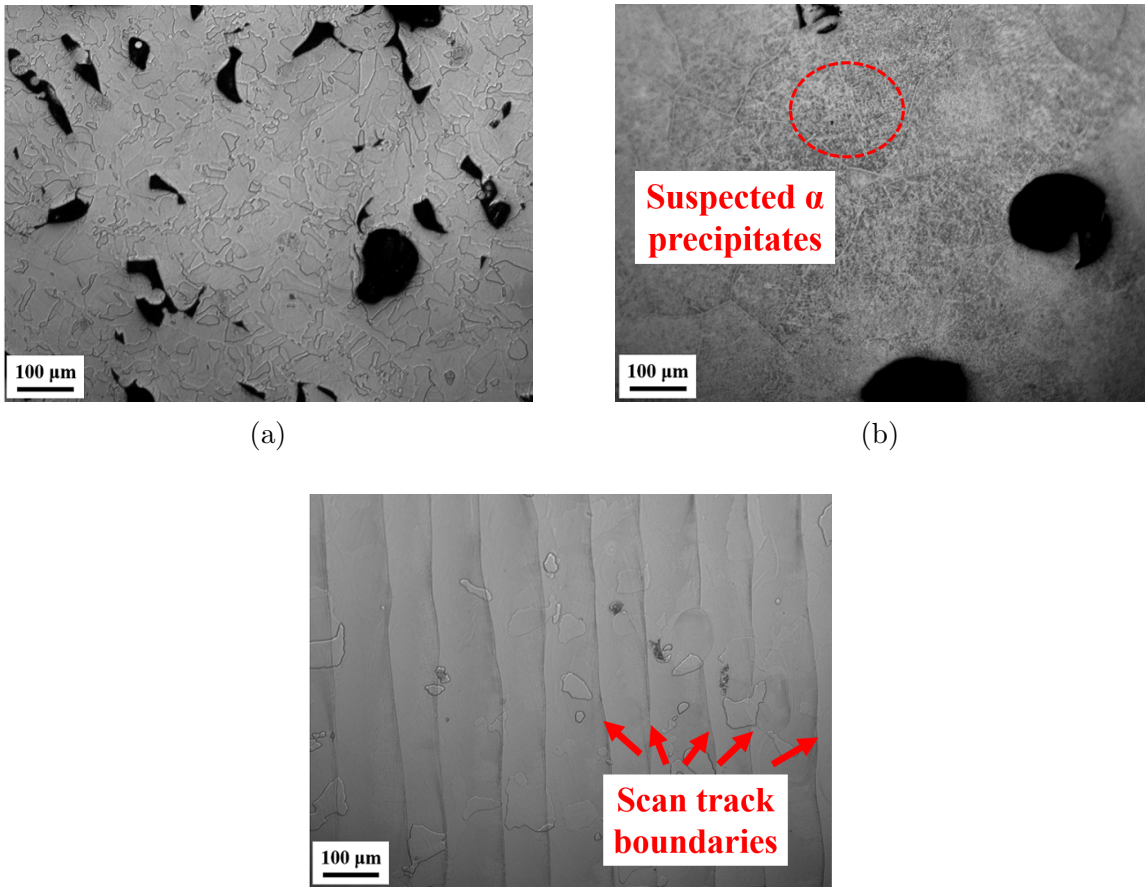

(a) (b)

(c)

Figure 4.21: The top view OM images showing (a) the lowest VED, (b) the highest VED and (c) the best density samples, respectively.

Several different defects occurred in the low VED samples are shown in Figure 4.22. Due to a lack of fusion, a fraction of powder particles are not melted, see Figure 4.22a.

In addition, some particles are partially melted, *i.e.* share a grain with the matrix while the fine dendritic grain structure inside the particles are almost intact as shown in Figure 4.22b. Finally, a number of particles were marked as embedded powder in the matrix by surface fusion. The evidence verifying their presence is the change of grain structure and a local area. As demonstrated in Figure 4.22c, the grain structure in the middle perfectly matches that of powder particles. This anomaly can result in poor mechanical response in general. However, it was validated by Vicker's micro-hardness test that the particle and the matrix show the same hardness which reduces the chance of observing different deformation behaviors from them.

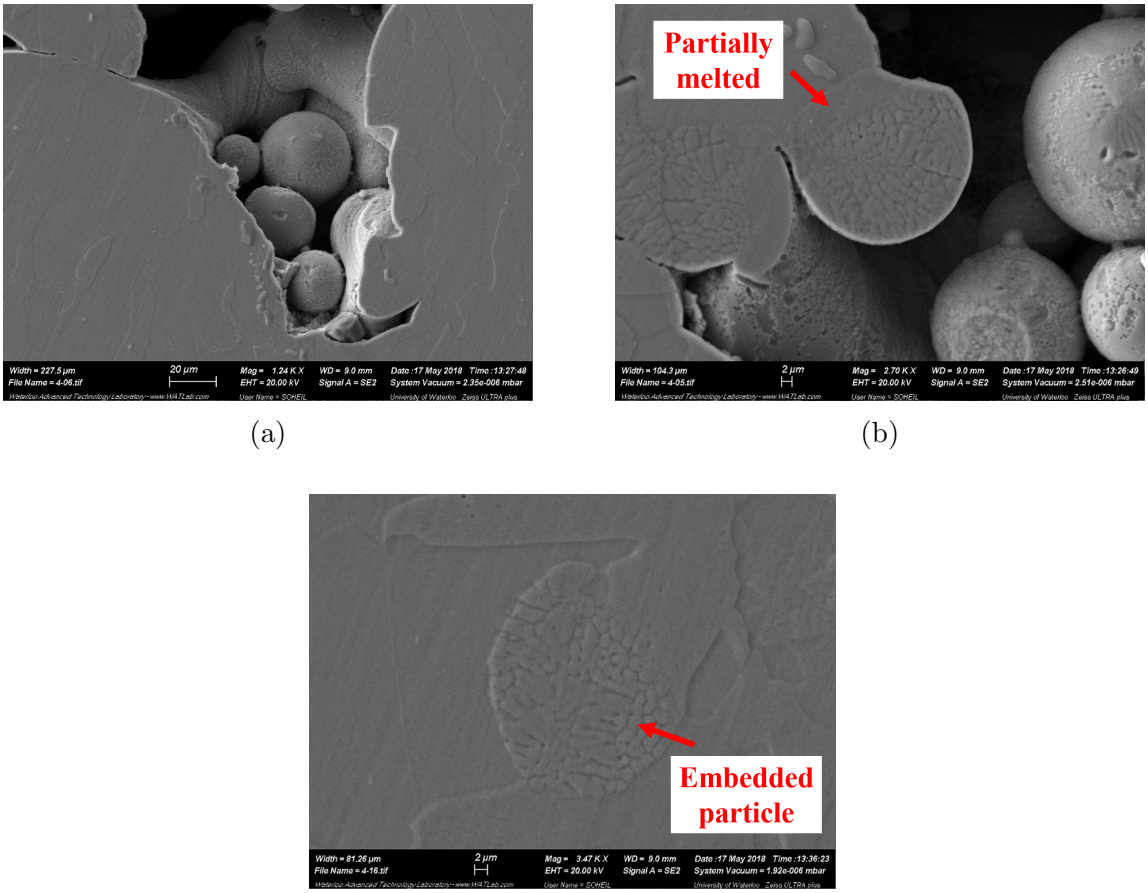

(a) (b)

(c)

Figure 4.22: The SEM images showing (a) unmelted powders, (b) partially melted powders and (c) embedded powders, respectively.

Figure 4.23 provides a closer look at the precipitates detected in the high VED sample. One can detect a thick continuous array of grain boundary alpha phase (α_{GB}) with a precipitate-free zone (PFZ) around the boundary. In addition, numerous nano-scale alpha precipitates, with the mean width of 73 nm, are detected within the matrix. Such HCP precipitates have grown in preferred directions which are expected to be coherent with the BCC matrix based on their sizes and alignment within the matrix. This theory will be assessed in detail via TEM results.

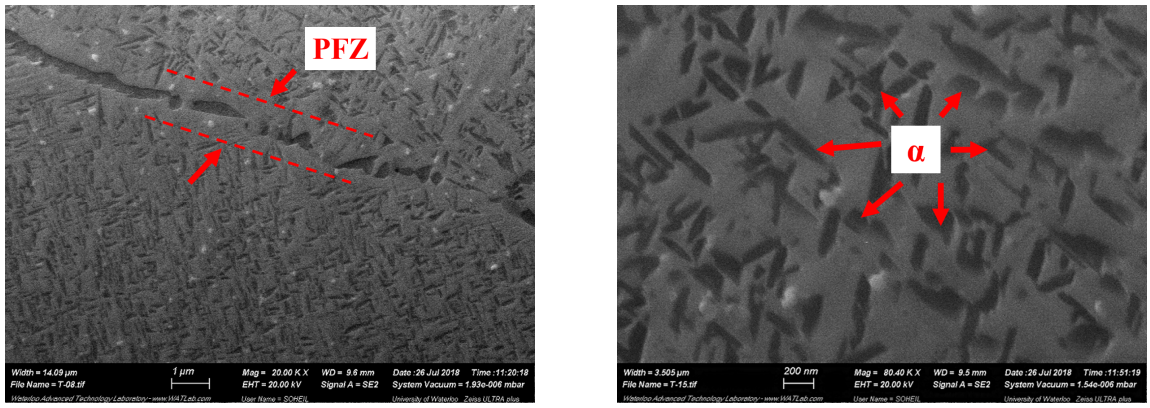

(a) (b)

Figure 4.23: The SEM images showing the precipitate particles in (a) low and (b) high magnifications.

Figure 4.24 demonstrates some microstructural features observed in the best VED sample. For instance, the epitaxial growth of grains along the building direction is clearly seen in Figure 4.24a. As explained before, this phenomenon occurs due to the recrystalization of the previously printed layers while the new layer is being printed leading to a columnar grain structure. In addition, it is observed that there is a shift from planar to cellular solidification at the melt pool edges, see Figure 4.24b. A similar transition is reported by Schwab *et al.* [4]. This transition can be attributed to the two main factors of temperature gradient (G) and growth rate (R) where a high $\frac{G}{R}$ ratio results in a planar solidification. The transition to the cellular solidification takes place as the ratio drops due to a decrease in temperature gradient.

Moreover, a few embedded powders were detected inside the best density sample. As discussed before, although these kinds of defects generally lead to a localized weak mechanical response, the side-effects will not be as severe in this case since no hardness variation was seen between the embedded powders and the matrix and the powders are not brittle.

However, the sudden change of grain structure at a local area might adversely affect the properties. The presence of such powders can be attributed to the local spattering or entrapment of powders into the pores and voids of the previously printed layer [54].

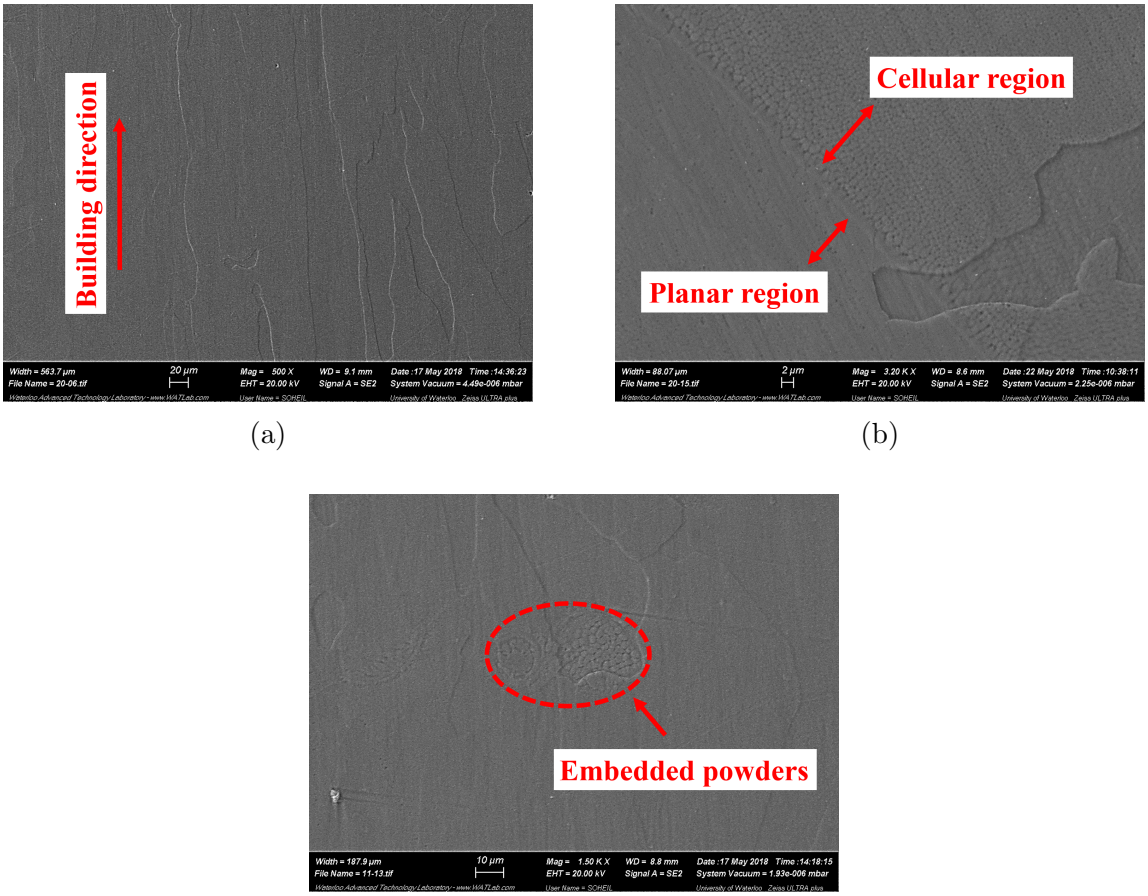

(a) (b)

(c)

Figure 4.24: The SEM images taken from the best density sample showing (a) the epitaxial growth of grains, (b) the transition in the solidification mechanism around the melt pool edges and (c) the embedded powders, respectively.

Figure 4.25 shows some features detected by the TEM observation of the sample with the best density. A high number of possible stacking faults are seen within the matrix. As it is clear in Figure 4.25a, the direction of the stacking faults changes from one grain to another due to the fact that different grains have different crystal orientations. In addition, one may see a nano-scale secondary phase distributed homogeneously in each grain, see

Figure 4.25b. Based on the size and morphology of this phase, *i.e.* finer than 30 nm and equiaxed, it can be considered as possible omega phase [55].

Considering that fact that the beta to alpha transformation has two-steps, as described before in Chapter 2, one can conclude that the best density sample, *i.e.* VED of 112 J/mm^3, is in the early stages of aging, *i.e.* the formation of the coherent omega phase with the HCP crystal structure and a short c/a ratio. Figure 4.25c appears to exhibit evidence of

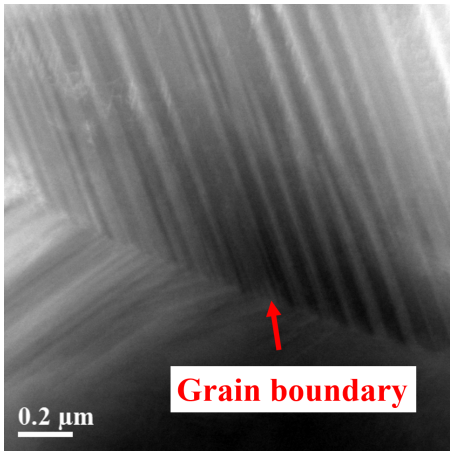

(a)

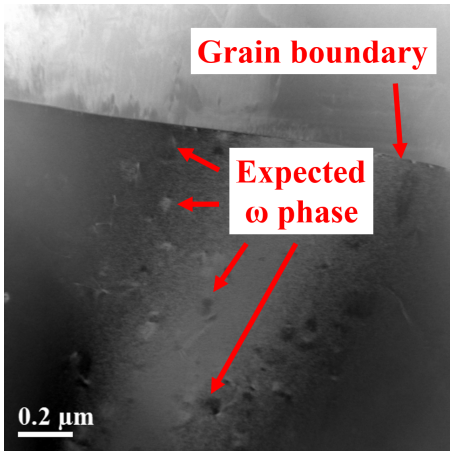

(b)

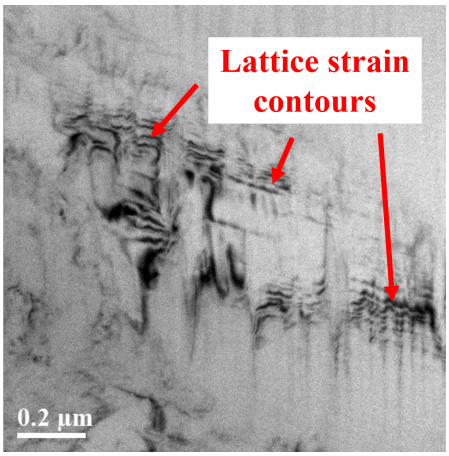

(c)

Figure 4.25: The TEM images taken from the best density sample showing (a) the stacking faults, (b) the HCP omega phase particles and (c) the lattice strains, respectively.

lattice strains in the BCC beta matrix, consistent with the very first stage in the beta to omega transformation. In summary, the sample has undergone an in-situ precipitation hardening, but contrary to the high VED sample, the precipitation is homogeneous leading to the hardness uniformity.

The presence of the omega phase in this sample is verified by the SAD diffraction pattern shown in Figure 4.26. One can clearly see the spots indicating the coherent omega precipitates. A similar pattern was observed by Zheng *et al.* [55]. The presence of such particles can facilitate post aging, which is commonly used as a subsequent heat-treatment process after the printing phase. These particles can act as preferential nucleation sites for alpha needles due to their higher energy level compared to the matrix which provides a share of the activation energy of nucleation and growth of the secondary phase, *i.e.* alpha.

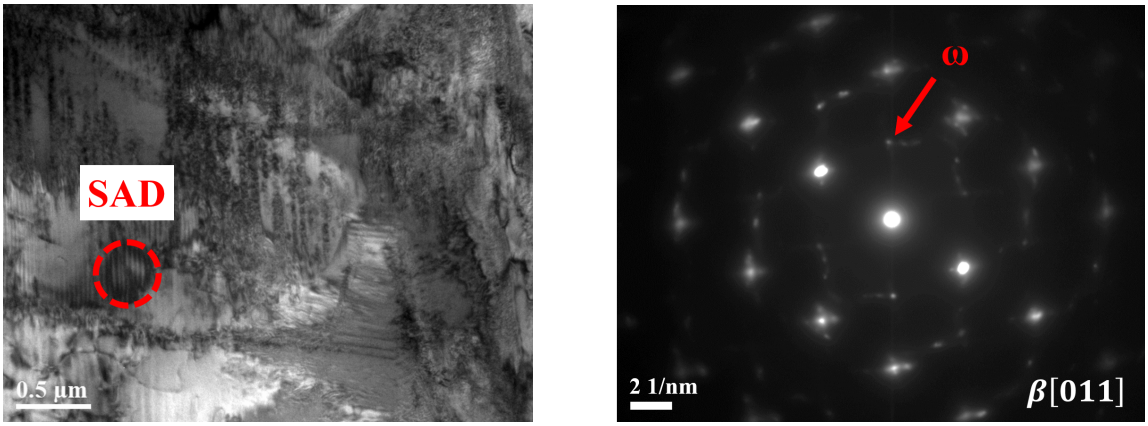

(a) (b)

Figure 4.26: The omega phase detection by TEM (a) the image taken from the SAD and (b) the diffraction pattern.

As it is shown in Figure 4.27, the beta to alpha transformation appears to be completed in the highest VED sample, *i.e.* VED of 584 J/mm^3. The common basket-wave structure is clearly seen in both the top and the bottom of the sample. However, one may notice that the alpha needles are significantly coarser at the bottom. In fact, the first few layers printed have undergone a much higher number of re-heating cycles which provides conditions for the growth of the alpha phase. In other words, the bottom part of the printed sample has received a higher amount of heat elevating the energy state of the matrix. Considering that the growth phenomenon is diffusion-based, the higher the heat input is, the faster it progresses. Thus, the growth of the alpha phase is expedited at the bottom of the sample.

By measuring the mean width of the alpha needles, one may realize that the top part is at the final stages of the omega to alpha transformation. While no equiaxed particles, *i.e.* the omega phase, is detected, the mean width size of less than 30 nm measured, see Figure 4.27a, which indicates that the needles have not started to coarsen. On the other hand, the mean width of 95 nm, see Figure 4.27b, implies that the alpha phase is in the final stages of growth in the bottom of the specimen.

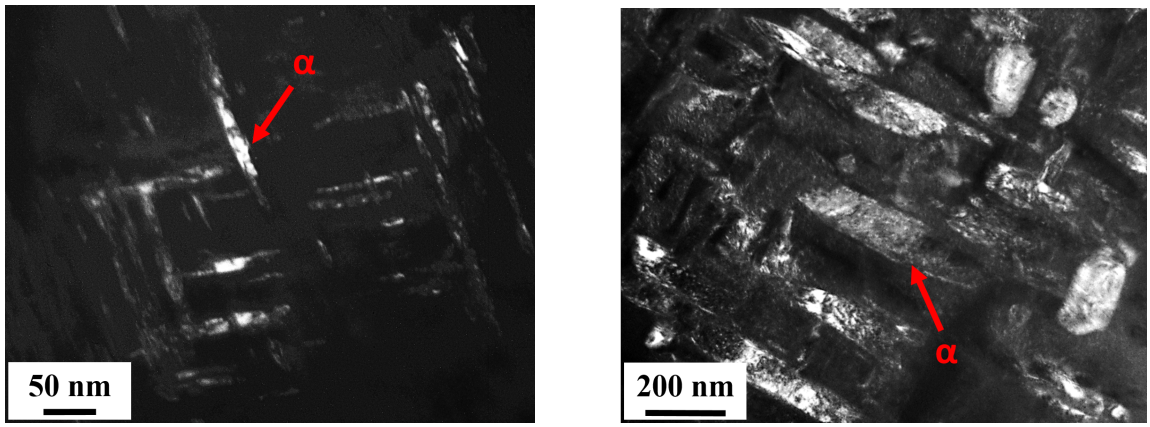

(a) (b)

Figure 4.27: The TEM images showing the alpha phase structures in (a) the top and (b) the bottom part of the sample with the highest VED, respectively.

Figure 4.28 shows the TEM diffraction pattern of a single alpha needle matching with the $\alpha[0001]$ zone axis. In addition, Figure 4.29 provides the TEM/EDAX color map of the alloying elements in order to understand the beta to alpha transformation. The alpha needles are observed in the primary image. One may notice that the titanium and aluminum content has not changed very much from one area to another. In contrast, it is clear that the needles are depleted from vanadium, molybdenum and chromium. Since all three of these elements are beta stabilizers, the needles transform into the HCP alpha phase controlled by the alpha stabilizer aluminum.

A comparison between the diffraction patterns of a pure beta matrix and the beta/alpha structure is made in Figure 4.30. While both patterns are taken from the same beta zone axis of $\beta[\bar{1}, 1, 1]$, Figure 4.30c shows the coherent alpha phase spots in between the bigger beta spots. In order to clarify the electron diffraction from multiple phases, Figure 4.30d provides a schematic illustration of the diffraction pattern of SAD 2. One may notice that the alpha needles have grown in three different preferred directions coherent with the matrix. The zone axis of the alpha phase is expected to be $\alpha[2\bar{1}\bar{1}0]$ as previously discussed

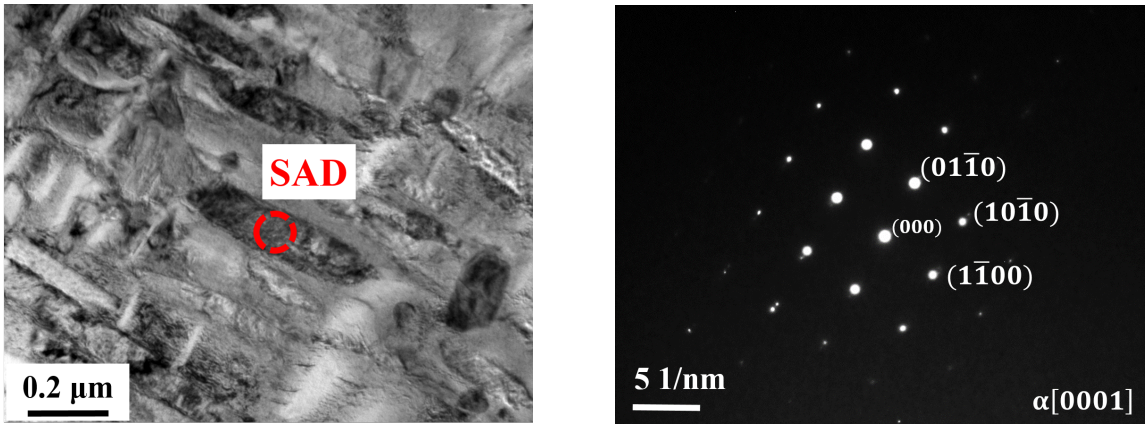

(a) (b)

Figure 4.28: The TEM observation of the alpha phase showing (a) the image taken from the SAD and (b) the the corresponding diffraction pattern, respectively.

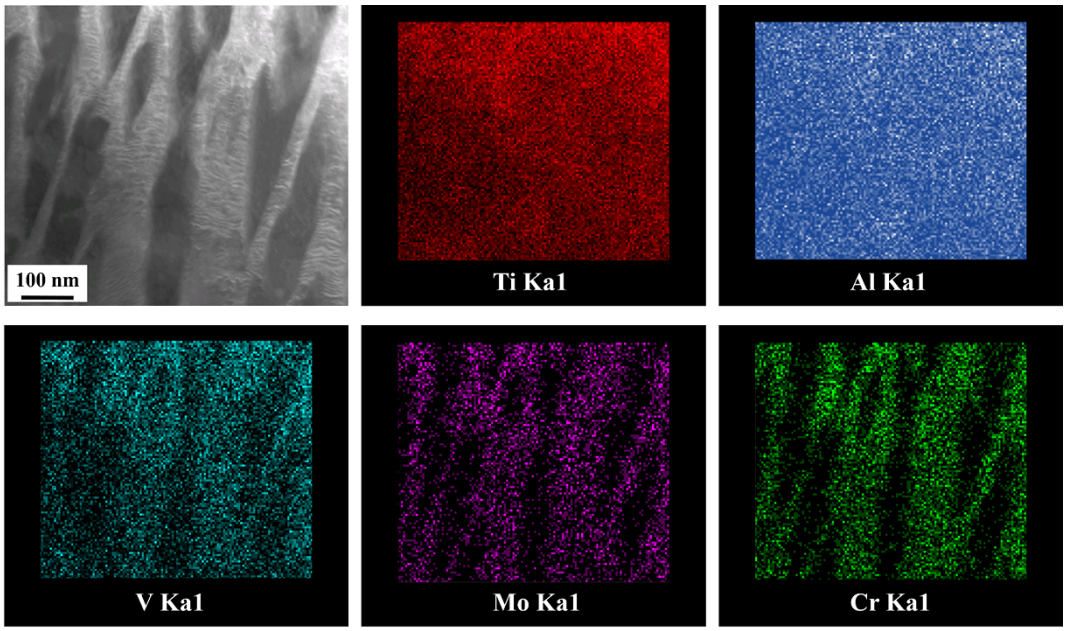

Figure 4.29: The TEM/EDAX color map showing the distribution of the alloying elements in the high VED sample.

by Schwab *et al.* [6]. In some cases, each two alpha spots overlap with a bigger beta spot

which can be seen as the so-called "satellite spots" in the diffraction pattern of SAD 2. This matter is shown in the schematic illustration as the intersection of the lines. One can detect the three primary growth directions of the alpha needles in Figure 4.30a.

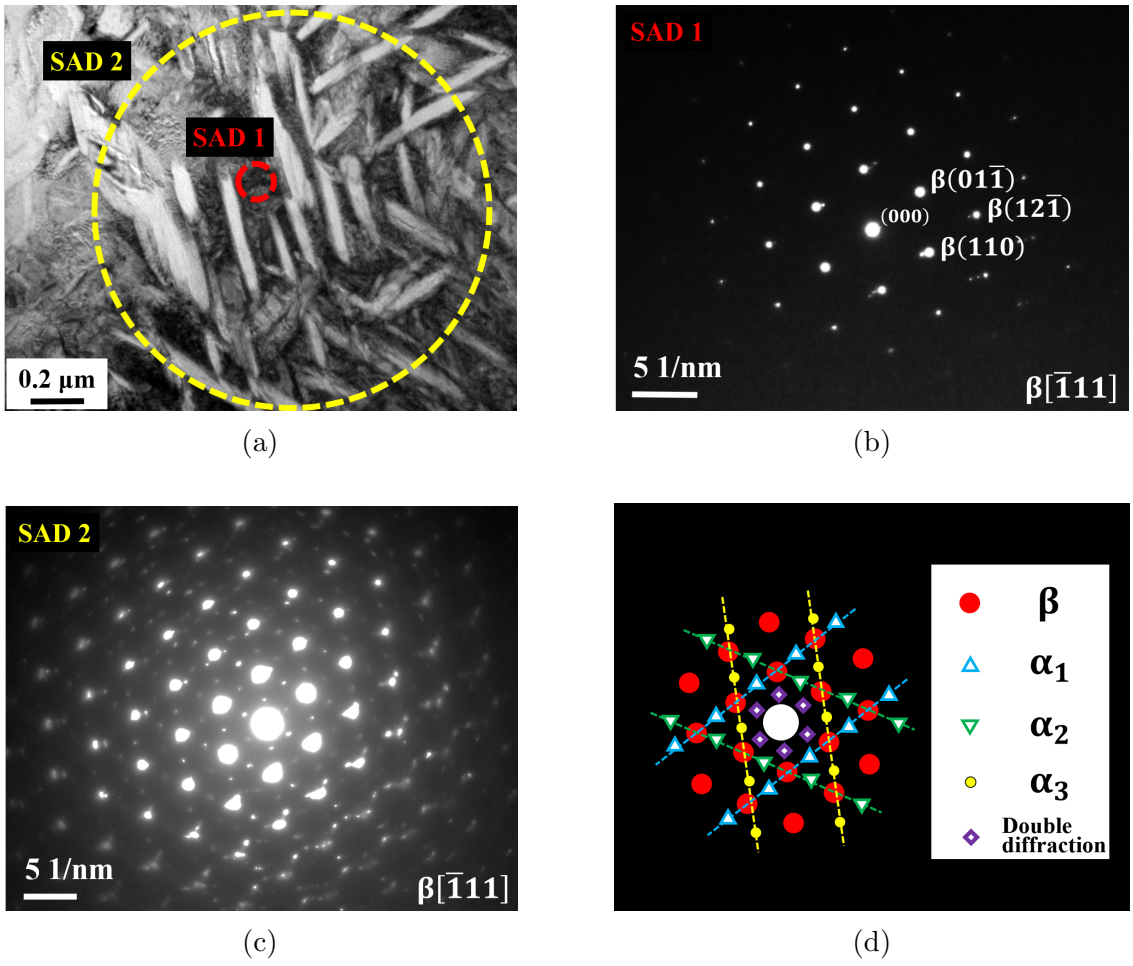

Figure 4.30: The comparison between the diffraction patterns of the pure beta phase matrix and the general overview of the structure: (a) the TEM image showing the SADs, (b) the diffraction pattern of SAD 1 showing a pure beta phase, (c) the diffraction pattern of SAD 2 showing the coherent alpha phase along with the matrix and (d) the detailed schematic illustration of the alpha phase pattern distribution in c.

The IPF color map of the last printed layer, *i.e.* top surface, of the best density sample is demonstrated in Figure 4.31. It shows a highly textured pattern and most of the grains have an orientation between (001) and (111) shown by pink. The pole figures presented

in Figure 4.32a verifies this theory by showing the grains are aligned strongly in a specific direction with a maximum of about seven times of the random intensity. The $< 100 >$ is usually the easy-growth direction for most of Titanium alloys [56]. More texture analysis is needed to fully discuss the reason why this direction is not the dominant one in this research.

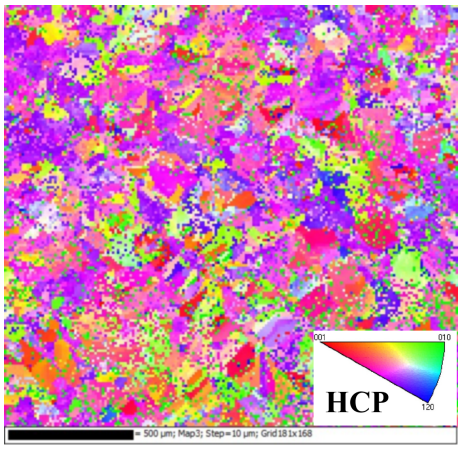

Figure 4.31: The IPF color map showing the texture of the top surface of the best density sample.

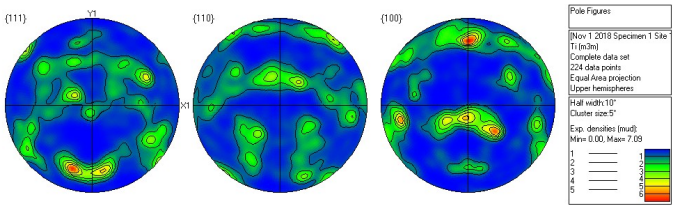

(a)

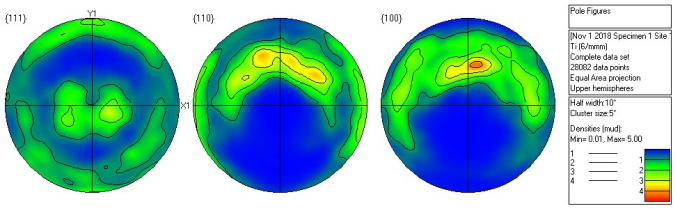

(b)

Figure 4.32: The pole figures of (a) the BCC and (b) the HCP phases, respectively.

Another aspect requiring more research is the fact that the volume fraction of the HCP phase, *i.e.* alpha, reported by the EBSD investigation is much higher than that of the TEM and XRD analyses. The HCP data points are 100 times more frequent than the BCC ones which suggests that the alpha phase is dominant, see Figure 4.32. However, the pole figures presented in Figure 4.32b also verifies that the material is highly textured. Since the hardness maps shown previously in Figure 4.19 supports the TEM and XRD results, it can be concluded that further texture analysis would be useful to explain the fraction of phases measured by EBSD.

4.3 Effect gemetry and scanning strategy

Figure 4.33 shows the second printing batch. As discussed in Chapter 3, the samples were printed in two geometries, *i.e.* cubic and cylindrical, and randomly distributed on the build plate. For each geometry, three scanning strategies, *i.e.* stripes, chessboard and total fill, were used and two identical samples of A and B were allocated for each combination of geometry and scanning strategy. In contrast to the first batch, no oxidized surface was detected while examining the samples, as they were all printed with the same VED of $112\,\mathrm{J/mm^3}$, *i.e.* the optimized VED.

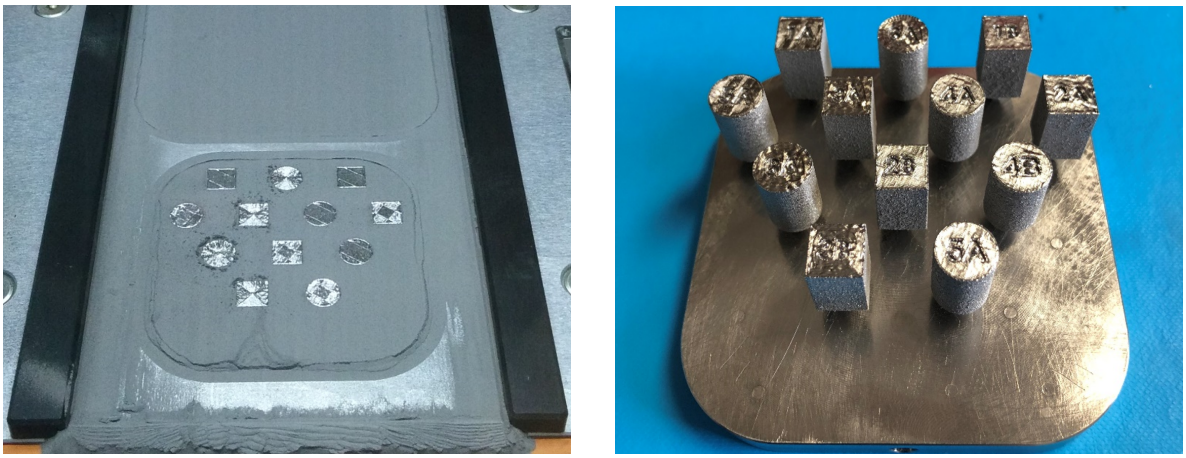

(a) (b)

Figure 4.33: The second printing batch showing the build plate (a) during the process and (b) after the process, respectively.

The effect of geometry and scanning strategy on the achieved relative density is pre-

sented in Figure 4.34. One may see that the total fill strategy leads to a poor density of less than 99% while stripes and chessboard show a similar density of more than 99.5%. In addition, the effect of geometry is negligible and there is no trend to prove that one geometry has an advantage over the other one.

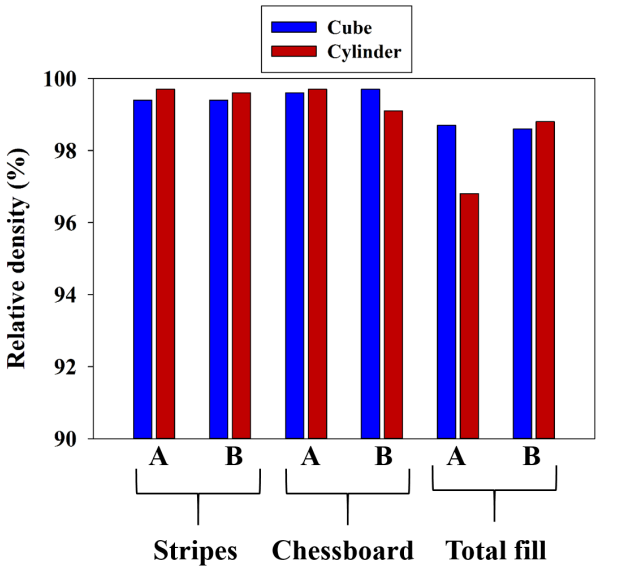

Figure 4.34: The effect of using different scanning strategies and geometries on the relative density.

In order to compare the stripes and chessboard strategies with higher accuracy, Figure 4.35 demonstrates the Nano-CT scan result. It is apparent that the chessboard strategy leads to a relatively high density of 99.94%. This is the best density achieved amongst all the first batch and second batch samples. In addition, it is observed that the pores are distributed homogeneously in both samples, however, one may notice that the chessboard strategy achieves a finer pore volume distribution compared to the stripes, 99.94% vs. 99.74%.

As shown in Table 4.4, the stripes and chessboard strategies produce the same hardness of $27 HR_c$, while the total fill strategy shows a slightly higher hardness number. This might be due to an in-situ heat treatment occurred during the printing process, however, the effects are not as severe as using a high VED. All these scanning strategies have their own specific printing pattern which, in some local areas, affect the frequency and duration of the re-heating cycles. This theory will be discussed further while investigating the corresponding microstructure of each strategy.

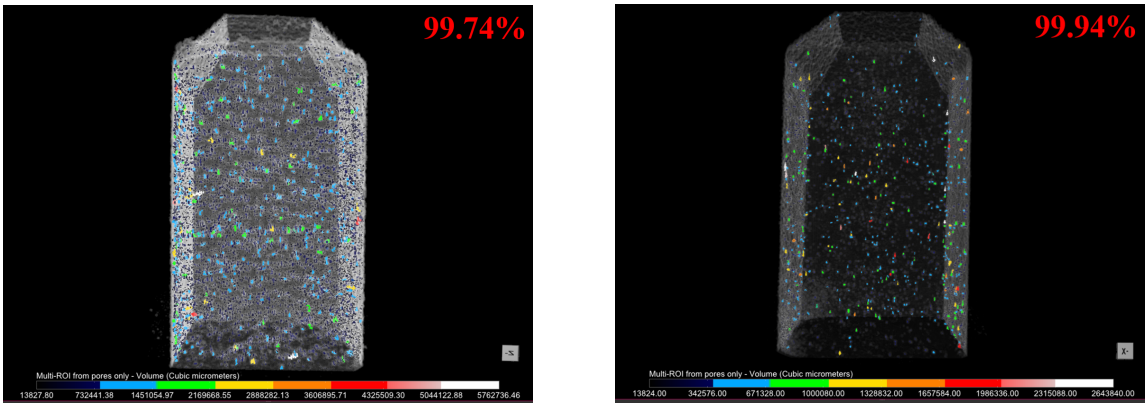

(a) (b)

Figure 4.35: The Nano-CT scan results showing the pore volume distribution when using (a) the stripes and (b) the chessboard scanning strategies, respectively.

Table 4.4: Rockwell hardness test results performed on the samples printed by the Stripes, Chessboard and Total fill scanning strategies

Scanning strategy	Sample #	Hardness number (HR_c)
Stripes	1A	27
Chessboard	2A	27
Total fill	3A	31

The front view cross-section of the samples are shown in Figure 4.36. The stereo microscopy images support the fact that the total fill strategy results in a very low density and the worst surface quality. One may see two vertical arrays of pores at the sides of the sample indicating a patterned porosity distribution, leading to a poor mechanical response.

Although the stripes strategy seems to have a better quality, in terms of lower porosity level, in this specific cross-section, the Nano-CT scan results presented previously in Figure 4.35 prove the higher density of the chessboard sample. In addition, the stripes sample seems to have a smoother surface compared to the one printed by the chessboard strategy.

Figure 4.37 shows the top view cross-section of the samples. One may see an "X" sign matching with the diagonals of the sample printed by the total fill strategy as a consequence of the patterned porosity. This can be attributed to the scanning path of this strategy. As shown previously in Figure 3.2, there is a sudden 90 degrees turn in the laser scan path occurring at the diagonals. The laser remains powered while making that turn, and in

turn, gives rise to spattering.

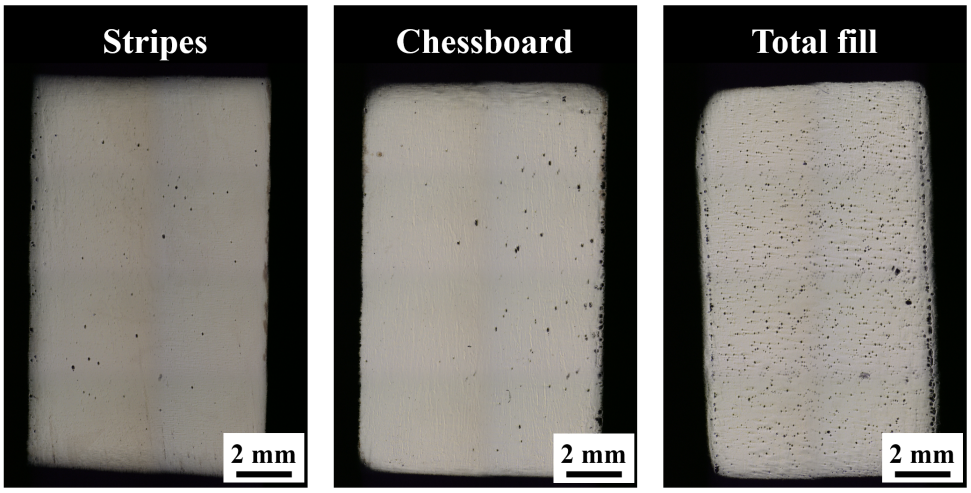

Figure 4.36: The stereo microscopy images showing the porosity level and surface condition of the printed samples with different scanning strategies in front view.

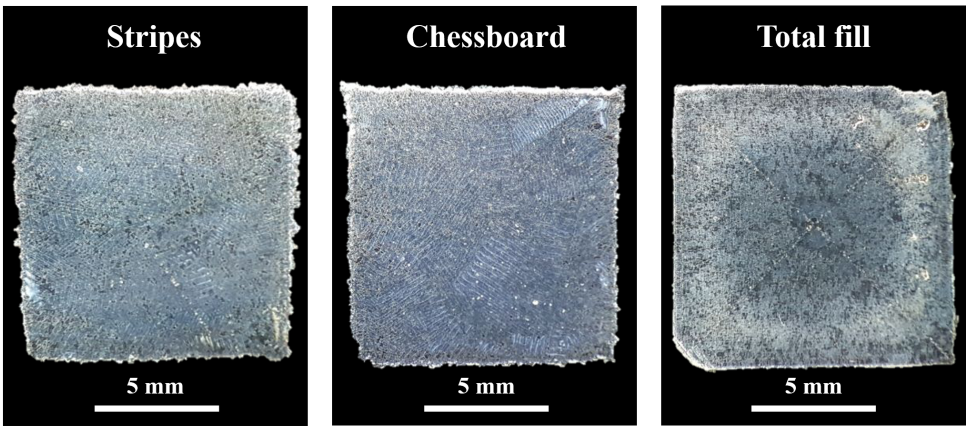

Figure 4.37: The stereo microscopy images showing the porosity level and surface condition of the printed samples with different scanning strategies along the top view.

The scanning tracks are partially seen in the strips and chessboard samples. As explained before, the images are showing a plane intersecting with 2 or 3 printed layers since it is not easy to section the samples with perfect alignment with the build layers. That is why the tracks are overlapping with each other in the images. Since the samples are etched,

one may notice a difference in the texture from one sample to another. This difference will be highlighted in detail while discussing the OM observations.

The OM images taken from the front view cross section of the samples are shown in Figure 4.38. Each melt pool array represents a printing layer and the building direction is vertical from the bottom to the top. One may note a high number of large pores in the sample printed by the total fill strategy. The highly textured and columnar grain structure is evident in all of the samples. As discussed before, this texture occurs as a consequence of the re-heating cycles.

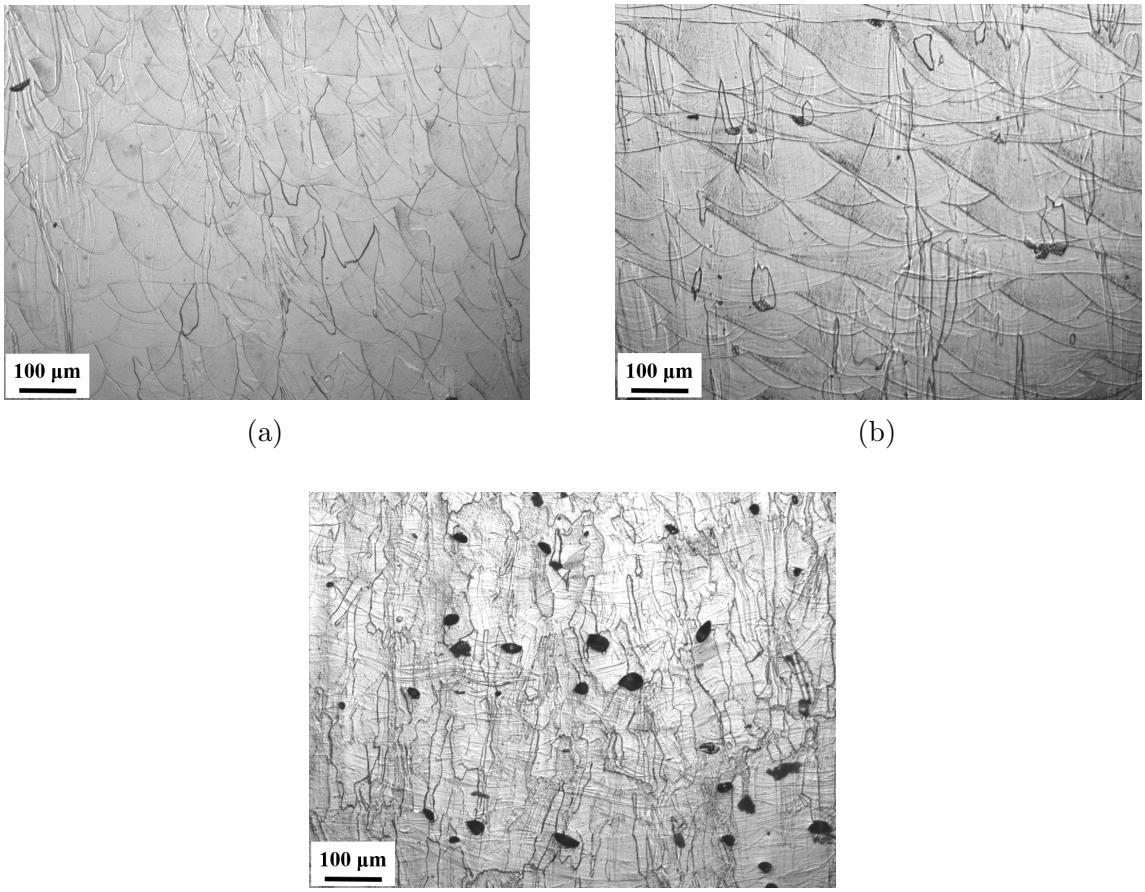

(a) (b)

(c)

Figure 4.38: The front view OM images showing the samples printed by (a) the strips, (b) the chessboard and (c) the total fill scanning strategies, respectively.

In addition, there is a difference between the melt pool geometries of the stripes and the

chessboard samples in terms of penetration and shoulder-to-shoulder width. Figure 4.39 highlights this difference by providing two OM images taken at the same magnification showing the melt pool shape of the last printed layer, *i.e.* the layer with no re-heating experience, of the stripes and the chessboard strategies. It is observed that the stripes strategy leads to a higher penetration compared to the chessboard strategy, *i.e.* 75 µm and 45 µm respectively. Considering that both samples were printed with the same VED, the melt pool shape is determined by the frequency and duration of the re-heating cycles. Based on their specific laser paths, see Figure 3.2, the interval between each time the laser scans a particular area varies between the two strategies, which directly affects the heat input applied to that area. The higher the heat input is, the higher the penetration.

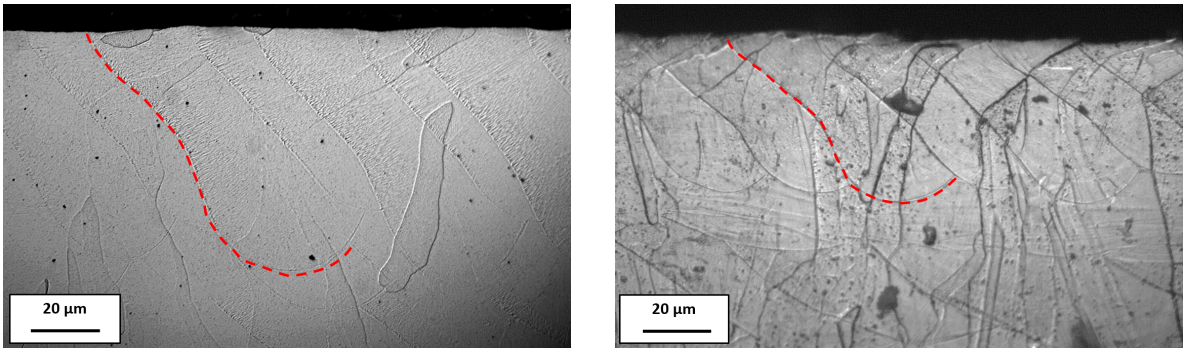

(a) (b)

Figure 4.39: The OM observations showing the melt pool geometries of (a) the stripes and (b) the chessboard scanning strategies, respectively.

Moreover, Figure 4.40 shows the top view cross-section of the samples. One may see the "X" mark in the total fill sample. As described before, this defect is an artifact of the sudden 90 degree turn in the laser scanning path while the laser is still on. In addition, the grain structure of the total fill sample is observed to be much coarser compared to the other two strategies. This can be explained by the fact that, as shown in Figure 3.2, the total fill scanning pattern starts from the very outer edges of the samples and ends at the center. This pattern leads to a high amount of heat accumulated at the center of each layer. Consequently, the grain structure is coarser at the center compared to the sides of the sample.

Finally, using the stripes and the chessboard strategies result in different grain structure. It is evident by comparing Figures 4.40a and 4.40b, the track lines are less clear in the sample printed by the stripes strategy. However, the scanning direction is inferred by looking at the grain structure. The grain size is observed to be the finest when the chessboard

strategy is used. EBSD analysis is required to fully compare the textures corresponding to each strategy.

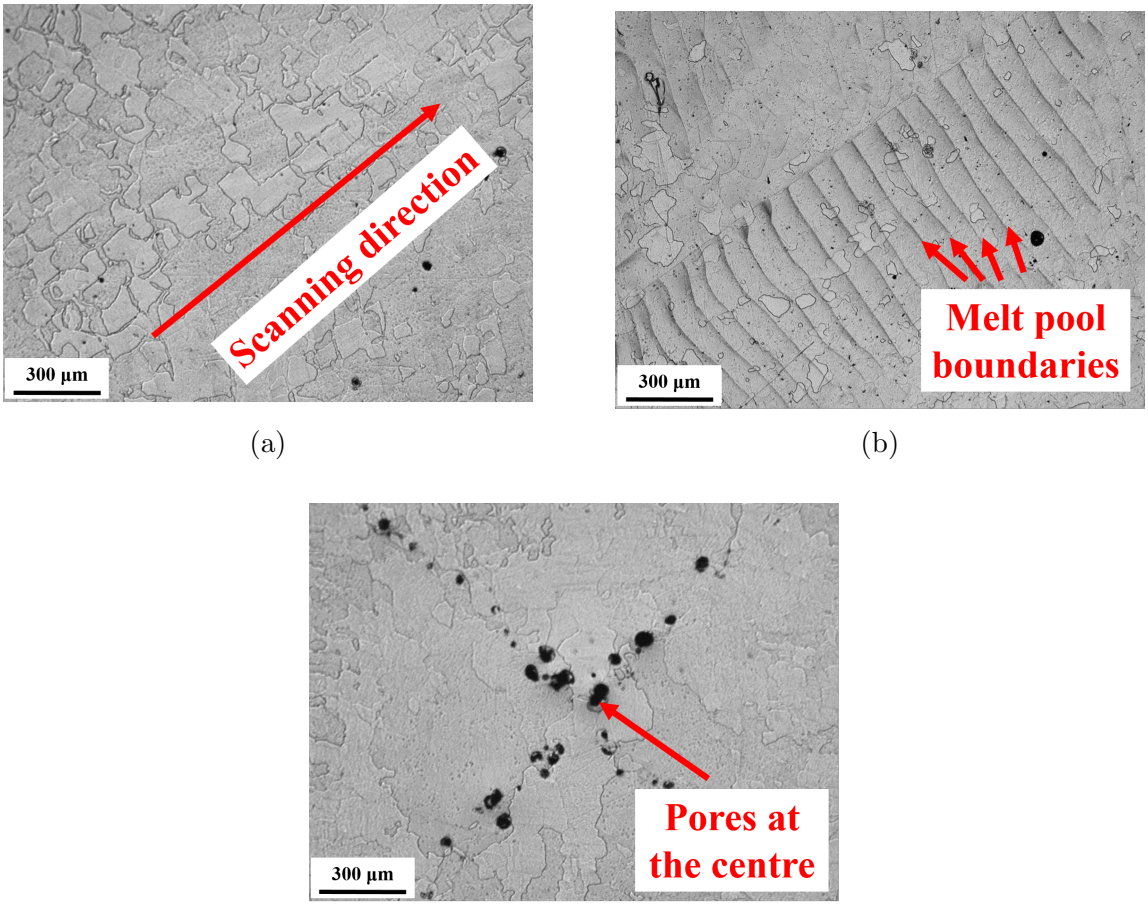

(a) (b)

(c)

Figure 4.40: The top view OM images showing the samples printed by (a) the strips, (b) the chessboard and (c) the total fill scanning strategies, respectively.

Chapter 5

Conclusion

In this research, the printability of Ti-5%Al-5%V-5%Mo-3%Cr by Selective Laser Melting (SLM) is studied. To this end, first the as-received powder was characterized thoroughly in terms of the chemical and physical properties as well as the microstructure associated with it. The effects of Volumetric Energy Density (VED), sample geometry and different scanning strategies on the density, surface roughness, hardness and microstructure of the printed parts were assessed. Archimedes and Nano-CT scanning tests were used to measure and compare the density of the parts with low and high accuracy, respectively. In addition, The surface roughness of the samples were investigated by mapping their surface profile with a laser confocal microscope. Moreover, the Rockwell and micro-Vickers hardness tests were performed, respectively, for the general hardness comparisons and the hardness color mapping. Finally, a detailed microstructural analysis was done using stereo microscopy, optical microscopy (OM), scanning electron microscopy (SEM), transmission electron microscopy (TEM), X-ray diffraction (XRD) and electron backscattered diffraction (EBSD) observations. A summary of the results is given below:

1. An optimized recipe is developed for the pulsed laser SLM of Ti-5553 resulting in the best density, surface roughness and hardness exceeding that of previous reports.

2. The recipe is modified to be used as an industrial manufacturing process. The suggested parameters such as the scanning velocity of 1.5 m/s and the laser power of 275 W meet the industry requirements regrading the production rate.

3. The β to α transformation is discussed in detail by TEM analysis identified the two step transition for the first time in a SLM printed part.

4. A comprehensive discussion is given regarding the effect of scanning strategies on the melt pool geometry and physical properties proving that the chessboard strategy is the best option for pulsed laser SLM of Ti-5553.

Chapter 6

Future works

Although the effects of Volumetric Energy Density (VED), sample geometry and scanning strategy were discussed in detail, there are still a few improvements that can be made in order to reach a more comprehensive and statistical results:

1. A narrower VED window can be chosen in the pre-determined optimized range and a new build plate can be designed to investigate the effect of VED within that range. The goal is to optimize the melt pool geometry by finding the transition from the goblet-like to the conductive melt pool shape.

2. More comprehensive EBSD analysis is needed to achieve a clear understanding of the texture corresponding with each scanning strategy. In addition, the texture analysis given for the best density sample needs to be improved to realize the reason of its conflict with the TEM and XRD results.

3. In order to industrialize the recipe, one should study the recyclablibity of the powder and investigate the effect of using a recycled powder instead of a virgin one.

4. The experimental work can be supported by Finite Element Analysis (FEA) of the process. This approach helps to study and predict the residual stresses associated with the modulated laser SLM in particular.

5. Based on the application, a series of static or dynamic mechanical testing is required. Once the optimized recipe is ready, one should start investigating the mechanical properties of the printed parts by performing tests such as tensile, compression, creep, impact or fatigue.

References

[1] Lutjering, *Titanium 2nd ed.* New York: Springer, 2007.

[2] T. Li, D. Kent, G. Sha, J. M. Cairney, and M. S. Dargusch, "The role of ω in the precipitation of α in near-β ti alloys," *Scripta Materialia*, vol. 117, pp. 92–95, 2016.

[3] Wikipedia, "Selective laser melting — Wikipedia, the free encyclopedia." [Online]. Available: https://en.wikipedia.org/wiki/Selective_laser_melting

[4] H. Schwab, F. Palm, U. Kühn, and J. Eckert, "Microstructure and mechanical properties of the near-beta titanium alloy ti-5553 processed by selective laser melting," *Materials & Design*, vol. 105, pp. 75–80, 2016.

[5] C. Zopp, S. Blümer, F. Schubert, and L. Kroll, "Processing of a metastable titanium alloy (ti-5553) by selective laser melting," *Ain Shams Engineering Journal*, vol. 8, no. 3, pp. 475–479, 2017.

[6] H. Schwab, M. Bönisch, L. Giebeler, T. Gustmann, J. Eckert, and U. Kuehn, "Processing of ti-5553 with improved mechanical properties via an in-situ heat treatment combining selective laser melting and substrate plate heating," *Materials & Design*, vol. 130, pp. 83–89, 2017.

[7] Tech-Labs, "Am400." [Online]. Available: https://tech-labs.com/products/am400

[8] A. Committee *et al.*, "Astm international committee f42-additive manufacturing technologies astm f2792-12 standard terminology for addititve manufacturing technologieswest conshohocken," 2009.

[9] T. Wohlers and T. Gornet, "History of additive manufacturing," *Wohlers report*, vol. 24, no. 2014, p. 118, 2014.

[10] W. E. Frazier, "Metal additive manufacturing: a review," *Journal of Materials Engineering and Performance*, vol. 23, no. 6, pp. 1917–1928, 2014.

[11] Statista, "Projected global additive manufacturing market size in 2015 and 2018 (in billion U.S. dollars)," 2018. [Online]. Available: https://www.statista.com/statistics/284863/additive-manufacturing-projected-global-market-size/

[12] I. Campbell, D. Bourell, and I. Gibson, "Additive manufacturing: rapid prototyping comes of age," *Rapid prototyping journal*, vol. 18, no. 4, pp. 255–258, 2012.

[13] R. Bogue, "3d printing: the dawn of a new era in manufacturing?" *Assembly Automation*, vol. 33, no. 4, pp. 307–311, 2013.

[14] J. Holmström, J. Partanen, J. Tuomi, and M. Walter, "Rapid manufacturing in the spare parts supply chain: alternative approaches to capacity deployment," *Journal of Manufacturing Technology Management*, vol. 21, no. 6, pp. 687–697, 2010.

[15] K. V. Wong and A. Hernandez, "A review of additive manufacturing," *ISRN Mechanical Engineering*, vol. 2012, 2012.

[16] S. H. Huang, P. Liu, A. Mokasdar, and L. Hou, "Additive manufacturing and its societal impact: a literature review," *The International Journal of Advanced Manufacturing Technology*, vol. 67, no. 5-8, pp. 1191–1203, 2013.

[17] A. A. Antonysamy, "Microstructure, texture and mechanical property evolution during additive manufacturing of ti6al4v alloy for aerospace applications," Ph.D. dissertation, The University of Manchester (United Kingdom), 2012.

[18] M. Peters, J. Kumpfert, C. H. Ward, and C. Leyens, "Titanium alloys for aerospace applications," *Advanced engineering materials*, vol. 5, no. 6, pp. 419–427, 2003.

[19] H. M. Flower, *High performance materials in aerospace*. Springer Science & Business Media, 2012.

[20] A. Uriondo, M. Esperon-Miguez, and S. Perinpanayagam, "The present and future of additive manufacturing in the aerospace sector: A review of important aspects," *Proceedings of the Institution of Mechanical Engineers, Part G: Journal of Aerospace Engineering*, vol. 229, no. 11, pp. 2132–2147, 2015.

[21] C. Leyens and M. Peters, *Titanium and titanium alloys: fundamentals and applications*. John Wiley & Sons, 2003.

[22] M. J. Donachie, *Titanium: a technical guide*. ASM international, 2000.

[23] I. Polmear, D. StJohn, J.-F. Nie, and M. Qian, *Light alloys: metallurgy of the light metals*. Butterworth-Heinemann, 2017.

[24] P. Kobryn and S. Semiatin, "The laser additive manufacture of ti-6al-4v," *Jom*, vol. 53, no. 9, pp. 40–42, 2001.

[25] J.-P. Kruth, M.-C. Leu, and T. Nakagawa, "Progress in additive manufacturing and rapid prototyping," *Cirp Annals*, vol. 47, no. 2, pp. 525–540, 1998.

[26] D. L. Bourell, M. C. Leu, and D. W. Rosen, "Roadmap for additive manufacturing: identifying the future of freeform processing," *The University of Texas at Austin, Austin, TX*, pp. 11–15, 2009.

[27] I. Gibson, D. W. Rosen, and B. Stucker, "Design for additive manufacturing," in *Additive Manufacturing Technologies*. Springer, 2010, pp. 299–332.

[28] K. Hon, "Digital additive manufacturing: From rapid prototyping to rapid manufacturing," in *Proceedings of the 35th International MATADOR Conference*. Springer, 2007, pp. 337–340.

[29] K. M. Taminger and R. A. Hafley, "Electron beam freeform fabrication for cost effective near-net shape manufacturing," 2006.

[30] P. Heinl, C. Körner, and R. F. Singer, "Selective electron beam melting of cellular titanium: mechanical properties," *Advanced Engineering Materials*, vol. 10, no. 9, pp. 882–888, 2008.

[31] O. L. Harrysson, O. Cansizoglu, D. J. Marcellin-Little, D. R. Cormier, and H. A. West II, "Direct metal fabrication of titanium implants with tailored materials and mechanical properties using electron beam melting technology," *Materials Science and Engineering: C*, vol. 28, no. 3, pp. 366–373, 2008.

[32] X. Li, C. Wang, W. Zhang, and Y. Li, "Fabrication and characterization of porous ti6al4v parts for biomedical applications using electron beam melting process," *Materials Letters*, vol. 63, no. 3-4, pp. 403–405, 2009.

[33] A. R. et al., "Lpbf recipe translation between continuous and modulated laser systems with different spot sizes," unpublished.

[34] A. B 822-17, "Standard test method for particle size distribution of metal powders and related compounds by light scattering," ASTM, Tech. Rep., 2017.

[35] A. E 1409-13, "Standard test method for determination of oxygen and nitrogen in titanium and titanium alloys by inert gas fusion," ASTM, Tech. Rep., 2014.

[36] A. E 1941-10, "Standard test method for determination of carbon in refractory and reactive metals and their alloys by combustion analysis," ASTM, Tech. Rep., 2016.

[37] A. E 2371-13, "Standard test method for analysis of titanium and titanium alloys by direct current plasma and inductively coupled plasma atomic emission spectrometry(performance-based test methodology)," ASTM, Tech. Rep., 2014.

[38] L. R. Samuel, "Rockwell hardness measurement of metallic materials," 2001.

[39] B. Taylor and E. Weidmann, "Metallographic preparation of titanium, struers application notes," *Struers Den. Rosendahls Bogtryk*, 2008.

[40] J. Clayton, "Optimising metal powders for additive manufacturing," *Metal Powder Report*, vol. 69, no. 5, pp. 14–17, 2014.

[41] Q. B. Nguyen, M. L. S. Nai, Z. Zhu, C.-N. Sun, J. Wei, and W. Zhou, "Characteristics of inconel powders for powder-bed additive manufacturing," *Engineering*, vol. 3, no. 5, pp. 695 – 700, 2017. [Online]. Available: http://www.sciencedirect.com/science/article/pii/S209580991730721X

[42] V. V. Popov, A. Katz-Demyanetz, A. Garkun, and M. Bamberger, "The effect of powder recycling on the mechanical properties and microstructure of electron beam melted ti-6al-4v specimens," *Additive Manufacturing*, 2018.

[43] H. Gong, K. Rafi, H. Gu, T. Starr, and B. Stucker, "Analysis of defect generation in ti–6al–4v parts made using powder bed fusion additive manufacturing processes," *Additive Manufacturing*, vol. 1, pp. 87–98, 2014.

[44] K. Morasch and D. Bahr, "The effects of hydrogen on deformation and cross slip in a bcc titanium alloy," *Scripta materialia*, vol. 45, no. 7, pp. 839–845, 2001.

[45] A. Dehghan-Manshadi and R. J. Dippenaar, "Development of α-phase morphologies during low temperature isothermal heat treatment of a ti–5al–5mo–5v–3cr alloy," *Materials Science and Engineering: A*, vol. 528, no. 3, pp. 1833–1839, 2011.

[46] W. Xu, M. Brandt, S. Sun, J. Elambasseril, Q. Liu, K. Latham, K. Xia, and M. Qian, "Additive manufacturing of strong and ductile ti–6al–4v by selective laser melting via in situ martensite decomposition," *Acta Materialia*, vol. 85, pp. 74–84, 2015.

[47] M. Tang, P. C. Pistorius, and J. L. Beuth, "Prediction of lack-of-fusion porosity for powder bed fusion," *Additive Manufacturing*, vol. 14, pp. 39–48, 2017.

[48] M. Rombouts, J.-P. Kruth, L. Froyen, and P. Mercelis, "Fundamentals of selective laser melting of alloyed steel powders," *CIRP Annals-Manufacturing Technology*, vol. 55, no. 1, pp. 187–192, 2006.

[49] G. Kasperovich, J. Haubrich, J. Gussone, and G. Requena, "Correlation between porosity and processing parameters in tial6v4 produced by selective laser melting," *Materials & Design*, vol. 105, pp. 160–170, 2016.

[50] B. Vrancken, L. Thijs, J.-P. Kruth, and J. Van Humbeeck, "Heat treatment of ti6al4v produced by selective laser melting: Microstructure and mechanical properties," *Journal of Alloys and Compounds*, vol. 541, pp. 177–185, 2012.

[51] T. Vilaro, C. Colin, and J.-D. Bartout, "As-fabricated and heat-treated microstructures of the ti-6al-4v alloy processed by selective laser melting," *Metallurgical and materials transactions A*, vol. 42, no. 10, pp. 3190–3199, 2011.

[52] E. Chlebus, B. Kuźnicka, T. Kurzynowski, and B. Dybała, "Microstructure and mechanical behaviour of ti—6al—7nb alloy produced by selective laser melting," *Materials Characterization*, vol. 62, no. 5, pp. 488–495, 2011.

[53] K. Amato, S. Gaytan, L. Murr, E. Martinez, P. Shindo, J. Hernandez, S. Collins, and F. Medina, "Microstructures and mechanical behavior of inconel 718 fabricated by selective laser melting," *Acta Materialia*, vol. 60, no. 5, pp. 2229–2239, 2012.

[54] E. Louvis, P. Fox, and C. J. Sutcliffe, "Selective laser melting of aluminium components," *Journal of Materials Processing Technology*, vol. 211, no. 2, pp. 275–284, 2011.

[55] Y. Zheng, R. E. Williams, J. M. Sosa, Y. Wang, R. Banerjee, and H. L. Fraser, "The role of the ω phase on the non-classical precipitation of the α phase in metastable β-titanium alloys," *Scripta Materialia*, vol. 111, pp. 81–84, 2016.

[56] B. Vrancken, L. Thijs, J.-P. Kruth, and J. Van Humbeeck, "Microstructure and mechanical properties of a novel β titanium metallic composite by selective laser melting," *Acta Materialia*, vol. 68, pp. 150–158, 2014.